

Reference constitutive model for Alloy 617 and 316H stainless steel for use with the ASME Division 5 design by inelastic analysis rules

Applied Materials Division

About Argonne National Laboratory

Argonne is a U.S. Department of Energy laboratory managed by UChicago Argonne, LLC under contract DE-AC02-06CH11357. The Laboratory's main facility is outside Chicago, at 9700 South Cass Avenue, Argonne, Illinois 60439. For information about Argonne and its pioneering science and technology programs, see www.anl.gov.

DOCUMENT AVAILABILITY

Online Access: U.S. Department of Energy (DOE) reports produced after 1991 and a growing number of pre-1991 documents are available free at OSTI.GOV (<http://www.osti.gov/>), a service of the U.S. Dept. of Energy's Office of Scientific and Technical Information

Reports not in digital format may be purchased by the public from the National Technical Information Service (NTIS):

U.S. Department of Commerce
National Technical Information Service
5301 Shawnee Rd
Alexandria, VA 22312
www.ntis.gov
Phone: (800) 553-NTIS (6847) or (703) 605-6000
Fax: (703) 605-6900
Email: **orders@ntis.gov**

Reports not in digital format are available to DOE and DOE contractors from the Office of Scientific and Technical Information (OSTI)

U.S. Department of Energy
Office of Scientific and Technical Information
P.O. Box 62
Oak Ridge, TN 37831-0062
www.osti.gov
Phone: (865) 576-8401
Fax: (865) 576-5728
Email: **reports@osti.gov**

Disclaimer

This report was prepared as an account of work sponsored by an agency of the United States Government. Neither the United States Government nor any agency thereof, nor UChicago Argonne, LLC, nor any of their employees or officers, makes any warranty, express or implied, or assumes any legal liability or responsibility for the accuracy, completeness, or usefulness of any information, apparatus, product, or process disclosed, or represents that its use would not infringe privately owned rights. Reference herein to any specific commercial product, process, or service by trade name, trademark, manufacturer, or otherwise, does not necessarily constitute or imply its endorsement, recommendation, or favoring by the United States Government or any agency thereof. The views and opinions of document authors expressed herein do not necessarily state or reflect those of the United States Government or any agency thereof, Argonne National Laboratory, or UChicago Argonne, LLC.

Reference constitutive model for Alloy 617 and 316H stainless steel for use with the ASME Division 5 design by inelastic analysis rules

Applied Materials Division
Argonne National Laboratory

September 2021

Prepared by

M. C. Messner, Argonne National Laboratory
T.-L. Sham, Idaho National Laboratory

Abstract

This report describes the development, calibration, and validation of an inelastic constitutive model describing the monotonic, cyclic, and creep behavior of Alloy 617 from room temperature to 983° C . The model is intended for incorporation into a new Nonmandatory Appendix to Section III, Division 5, Subsection HB, Subpart B of the ASME Boiler & Pressure Vessel Code providing guidance on developing models for use with the ASME design by inelastic analysis provisions as well as a listing of acceptable material models for each Class A material that designers can use without further validation. The report described the development of the A617 model as well as providing an updated draft appendix, ready for ASME ballot, incorporating the A617 and the previously-developed 316H model. The development of this appendix and the related material models will promote the widespread application of the generally more efficient inelastic analysis rules.

Table of Contents

Abstract	i
Table of Contents	iii
List of Figures	v
List of Tables	vii
1 Introduction	1
2 Base model: calibration against Code Case data at 950° C	3
2.1 Approach	3
2.2 Available data	4
2.3 The initial model	5
2.4 Comparison to data	6
3 Temperature scaling: extending the model to the full temperature range	13
3.1 Available data	13
3.2 Scaling parameters	13
3.2.1 Rate sensitivity and initial flow stress	14
3.2.2 Isotropic and kinematic hardening	16
3.2.3 Tertiary creep: Hayhurst-Leckie damage	17
3.3 Verifying the scaled models	19
3.3.1 Tensile curves	19
3.3.2 Creep curves	19
3.3.3 Fatigue and cyclic hardening	19
3.3.4 Cyclic hysteresis at 950° C	24
4 Validation comparisons	27
4.1 The final model	27
4.1.1 Rate equations	27
4.1.2 Model parameters	28
4.2 Validation tests	29
4.2.1 Comparison to abstracted test data	29
4.2.2 ASME isochronous stress-strain curves	31
4.2.3 Strain rate jump tests	32
4.2.4 Thermomechanical tests	35
4.2.5 Pressurized SMT tests	35
4.3 Model discrepancies	36
5 Conclusions	39
5.1 Summary of A617 modeling	39
5.2 Balloting progress	39
Acknowledgments	41
Bibliography	43
A Description of A617 and 316H material models for the ASME Appendix Z	47
A.1 316H	47
A.2 Alloy 617	50

List of Figures

2.1	Comparison between model predictions and tension test results at 950° C. (a) Raw comparison to experimental data; (b) comparison assuming a constant strain rate of $8.33 \times 10^{-5} \text{ s}^{-1}$	7
2.2	Comparison between the model and the available creep data (full creep curves) at 950° C.	8
2.3	Comparison between the test results and the model predictions for the fatigue and creep-fatigue tests at 950° C with $\Delta\epsilon = 0.3\%$. The subcaptions indicate the hold time for each test. The experimental data is blue, the model predictions orange.	8
2.4	Comparison between the test results and the model predictions for the fatigue and creep-fatigue tests at 950° C with $\Delta\epsilon = 0.6\%$. The subcaptions indicate the hold time for each test. The experimental data is blue, the model predictions orange.	9
2.5	Comparison between the test results and the model predictions for the fatigue and creep-fatigue tests at 950° C with $\Delta\epsilon = 1.0\%$. The subcaptions indicate the hold time for each test. The experimental data is blue, the model predictions orange.	10
3.1	Kocks-Mecking diagram for Alloy 617.	15
3.2	Difference between S_u and $1.25S_y$ as a function of temperature.	17
3.3	Linear Larson-Miller correlation used to fix the damage model parameters.	18
3.4	Comparison between the simulated and experimental tensile curves.	20
3.4	Comparison between the simulated and experimental tensile curves (continued).	21
3.5	Comparison between the simulated and experimental creep curves.	22
3.6	Cyclic hardening curves comparing the model to fatigue test at several different temperatures.	23
3.7	Reassessment of the model versus the 950° C creep-fatigue data.	25
4.1	Comparison between experimental yield strength measurements and the model prediction as a function of temperature.	29
4.2	Comparison between the experimental time to 1% strain data and simulated time to 1% data from the viscoplastic model.	31
4.3	Comparison between the Code Case N-898 (solid lines) and the model predicted (dashed lines) isochronous stress-strain curves. The times for the plots, from highest curve to lowest, are 0 hours (hot tensile curve), 1 hour, 10 hours, 1,000 hours, 10,000 hours, and 100,000 hours.	33
4.4	Comparison between experimental strain rate jump tests and the model predictions.	34
4.5	Comparison between the thermomechanical experiment and the model predictions. (a) Temperature profile imposed on the sample. (b) Comparison between the model and simulation stress history.	35
4.6	Sketch showing the p-SMT test geometry, loading, and the corresponding finite element model used here to compare the Alloy 617 material model to the experimental results.	36

4.7 Pressurized SMT simulation data.	37
--	----

List of Tables

2.1	Available experimental data at 950° C. We have complete records (full time-strain-stress-temperature histories) for all of these experiments. Records labeled “A617 CC” are from the Alloy 617 ASME Code Case qualification effort.	5
2.2	Calibrated parameters for the initial model at 950° C.	6
3.1	Standard experimental data for temperatures other than 950° C. Records labeled “A617 CC” are from the Alloy 617 ASME Code Case qualification effort. Records labeled “dedicated tests” are from a test campaign through the ART program specifically for calibrating the model discussed here. . . .	13
3.2	The temperature-dependent Young’s modulus of Alloy 617, per the ASME Code Case.	14
3.3	Kocks-Mecking parameters used in the final model. Parameters are all non-dimensional.	15
3.4	Calibrated Larson-Miller parameters and the Hayhurst-Leckie parameter ϕ defining the damage model.	18
4.1	Model parameters. Units are compatible with megapascals for stress, Celsius for temperature, and seconds for time.	30
A.1	Definition of mathematical symbols used to define the 316H model.	48
A.2	316H model parameters. Units are compatible with megapascals for stress, Celsius for temperature, and seconds for time.	49
A.3	Definition of mathematical symbols used to define the Alloy 617 model. . .	50
A.4	A617 model parameters. Units are compatible with megapascals for stress, Celsius for temperature, and seconds for time.	52

1 Introduction

Section III, Division 5, Subsection HB, Subpart B of the ASME Boiler & Pressure Vessel Code covers the design and construction of Class A high temperature reactor components. A unique feature of the high temperature Class A nuclear rules is that the rules require components meet strain accumulation and creep-fatigue damage criteria in addition to load-controlled design limits and buckling criteria. The Code provides two options for satisfying these criteria: design by elastic analysis and design by inelastic analysis. Of these two options, design by inelastic analysis historically produced less over-conservative designs [1] and was used in the design of components where the reactor operating conditions require an efficient structural design. While the ASME Code provides detailed acceptance criteria for the inelastic design method, it does not provide material models for use with the design method. Instead, the current Code rules require either the designer to develop and justify a suitable model as part of the Design Report or for the Owner to specify a model as part of the Owner's Design Specification. Developing a suitable model is not trivial, typically requiring a dedicated research program. As such, this current approach to developing models limits the future application of the more efficient inelastic analysis rules.

A new Nonmandatory Appendix to Subpart HBB of the Code providing guidance on developing suitable inelastic models as well as a collection of acceptable material models [2] has been developed under the US Department of Energy, Advanced Reactor Technologies (ART) Program. These models will provide a third option to designers: they can use the model described in the appendix without further justification. This new option would promote the wider use of the inelastic rules. The first version of this appendix, under ballot at ASME, includes the guidance on model development as well as a model for Grade 91 steel [2–5]. Additional work resulted in the development of a similar model for 316H stainless steel [6, 7]. This report describe the development and validation of a suitable model for the nickel-based Alloy 617 as well as a draft revised ASME proposal incorporating the A617 and 316H models.

The appendix outlines a number of criteria a model should meet to provide accurate stress analysis results for use with the ASME design rules:

- The model should capture average material properties considering heat-to-heat variation in the material response as well as experiment-to-experiment variations.
- The model must capture the cyclic response of the material, including the effect of holds at constant stress or strain. Typically creep-fatigue experiments are used to quantify this response.
- When used with the strain accumulation criteria or to develop a general model that can be used for both the strain accumulation and creep-fatigue criteria the model must capture all stages of creep deformation: primary, secondary, and tertiary.
- The model must capture the interaction of creep and plasticity. Typically this requires using a unified viscoplastic form, where a single viscoplastic rate equation represents both deformation mechanisms. However in the past a non-unified form has been used in conjunction with rules for coupling the internal variables describing material resistance between the rate-independent plastic and rate-dependent creep models.

- The model should accurately describe the material response under multiaxial load and under non-isothermal conditions.
- The model should be validated against experimental data covering the entire temperature range from room temperature to the ASME maximum use temperature (983° C for Alloy 617).

Developing such a model requires a large experimental database for calibrating the model and the results of several specialized, non-standard tests for validation.

Past work [8] assesses a constitutive model for Alloy 617 developed by Sham, Walker, and coworkers [9] against these criteria¹. We concluded that while the model was sufficiently accurate at very high temperatures it was not sufficiently accurate over the entire ASME temperature range. Moreover, this model has a very complicated, non-standard form with a large number of parameters. We recommended the development of a new model for Alloy 617 with better accuracy over the entire temperature range and with a simpler form.

This report describes the development, calibration, validation, and implementation of such a model. The model uses a comparatively simple, standard Chaboche form [10–13] and accounts for the material rate dependence, hardening/softening, and creep rate over the entire temperature range. We validate the model against a large collection of experimental results, including experiments quantifying the material response under multiaxial and non-isothermal load. The final model is suitable for incorporation into the Nonmandatory Appendix Z.

Chapter 2 develops a model form and calibrates the model parameters against a detailed collection of experimental tests at 950° C collected as part of the original Alloy 617 Code qualification effort by the ART program. These test records include the complete experimentally-measured time, strain, and stress data. Calibrating the model against detailed test data of this kind produces a very accurate description of the material, albeit only for 950° C. Chapter 3 discusses the challenges in applying this approach for the rest of the temperature range, where complete test data are not available. Instead we develop parameter scaling rules to alter the parameters calibrated at 950° C to capture the behavior of the material at the remaining temperatures. Chapter 4 then validates the final model against a large collection of test results not used in calibrating the original 950° C model or the temperature scaling rules. Chapter 5 summarizes the model development and validation work and describes plans for incorporating the model in the ASME Appendix Z. Appendix A of this report then provides an updated draft version of the appendix, ready for ballot at ASME, including the new A617 model and the previously-developed 316H model [6, 7].

¹Additional details on later work on the model provided by private communication with T.-L. Sham.

2 Base model: calibration against Code Case data at 950° C

2.1 Approach

Developing a suitable model for Appendix Z requires selecting a model form that can represent the available experimental data, finding an optimal parameter set for the model by calibrating against a database of experimental tests, and then validating the final model to ensure it will be robust when used to simulate conditions not in the test database.

In past work we calibrated models intended for use in the new Appendix Z described in the introduction using genetic algorithm optimization [2–7]. This approach has several advantages:

1. It does not require the model sensitivity – the gradient of the objective function to minimize with respect to the model parameters.
2. It is a flexible approach, making it comparatively easy to define the objective function to account for incomplete records of experimental tests. For example, in our past work we were able to calibrate models against abstracted cyclic test data given as plots of the maximum and minimum flow stress as a function of cycle count.
3. The structure of the algorithm makes it easy to parallelize.

However genetic algorithm optimization has significant disadvantages as well:

1. The optimization is slow in two senses. First, the genetic algorithm heuristic often requires a large number of iterations to reach an approximate global minimum. Secondly, algorithms maintain a population of models, meaning in each iteration the genetic algorithm must evaluate each experiment multiple times. These two factors multiply, i.e. if the population size is n_{pop} and the number of iterations n_{iter} then the total model evaluations required is $n_{pop} \times n_{iter}$, meaning it requires a large amount of computation time to find a optimized parameter set.
2. Genetic algorithm optimization is a heuristic – there is no mathematical guarantee that the algorithm will find a global or even local minimum. Developing models with the approach in our past work required carefully selecting the algorithm hyperparameters (i.e. the parameters describing how the GA functions, not the model parameters) and the starting population of initial guesses in order to achieve good results.

An additional significant disadvantage of the techniques used in our past work is that the optimization approach could only consider a few hundred loading cycles for cyclic tests, even for experiments that lasted 1000s of cycles. The reason is that the model time integration cannot be parallelized. Each load cycle requires a reasonable number (at least 30-40 in our experience) time integration steps to capture the details of the cyclic load history. Because this time integration cannot be parallelized it limits the number of load cycles that can be included in the optimization loop.

As part of a US Department of Energy award to Kairos Power, LLC through the U.S. Industry Opportunities for Advanced Nuclear Technology Development funding program, ANL developed a new constitutive model calibration software that uses a machine learning

backend called PyTorch [14] to evaluate the model, calculate the model sensitivity, and optimize the parameters. The package efficiently computes the model sensitivity using the adjoint method [15] and PyTorch’s built in Automatic Differentiation (AD) routines. Having the sensitivity available opens up the space of possible optimization algorithms. In particular, for calibrating a best-fit, deterministic model we find the L-BFGS algorithm can return a local minima in a very small number of iterations.

Our original plan for developing the A617 model described here was to apply our old, genetic algorithm approach. However, the new model calibration method is much more efficient than the GA method and tends to produce better, more accurate models. There are two reasons for this:

1. The L-BFGS algorithm is not a heuristic and will return an actual local minima.
2. The PyTorch implementation vectorizes both the forward model evaluations — i.e. running the model for each experiment — and the gradient calculation. Vectorizing here means that rather than run each experiment one at a time, sequentially instead the new implementation evaluates all the experiments at once. This, in effect, converts a series of scalar operations to a single large vector operations. Modern CPUs and GPUs can execute this type of blocking much more efficiently than scalar models, meaning the time required per time integration step is much shorter than our old implementation, particularly when running on the GPU. This means we can now afford to calibrate the model against the full record of the cyclic tests, using every load cycle.

We will publish a full description of this new calibration approach both in the GAIN project final report and in an upcoming journal publication.

The optimizer minimizes a squared error loss function to find an optimal parameter set:

$$loss = \sum_{j=1}^{n_{exp}} \sum_{i=1}^{n_{time}} (\sigma_{j,i}^{model} - \sigma_{j,i}^{experiment})^2 \quad (2.1)$$

where the outer sum is over each experiment in the database and the inner loop over each individual (time, strain, stress, temperature) measurement in the experimental record. The model is setup to be strain controlled: the forward model evaluation returns the stress given the strain, temperature, and time. Some of the tests (for example creep tests) are stress controlled. However, given that the model would produce the same results given the experimental strain and solving for stress or given the stresses and solving for the strains provided the model perfectly reproduces the experiment, only using strain control provides an adequate loss function — i.e. one that goes to zero as the model approaches perfect accuracy.

The downside of the new optimization approach is that it requires a complete record of each test – the full (time, strain, stress, temperature) history. This data is not often available from historical sources or the open literature.

2.2 Available data

However, we do have access to a large set of experimental results with complete test records. These experiments are part of the Alloy 617 Code Case qualification test campaign by the

Test type	Conditions	Number	Sources
Standard ten- sion	Performed per ASTM E21 [16]	2	A617 CC
Creep	Loading rates assumed to be 1 MPa/minute. Stress values of 16, 23, and 34 MPa.	4	A617 CC, [17]
Strain controlled- cyclic	$R = -1$ with tensile holds, combinations of 0.3%, 0.6% and 1.0% strain ranges and 0, 3, 10, and 30 minute hold times.	33	A617 CC

Table 2.1: Available experimental data at 950° C. We have complete records (full time-strain-stress-temperature histories) for all of these experiments. Records labeled “A617 CC” are from the Alloy 617 ASME Code Case qualification effort.

ART program, in addition to a few complete creep curves drawn from the literature. Table 2.1 lists the number and type of experiments available. All of these tests were conducted at 950° C. There are a few additional cyclic tests where we have complete test records at lower temperatures and there are complete records of tension and creep tests ranging from room temperature to 950° C. However, the vast majority of the A617 Code Case cyclic tests were done at 950° C. As such, we first develop a highly accurate model for Alloy 617 at 950° C and then extend it to the complete ASME temperature range (room temperature to 983° C, though we extend the model to 1000° C) by scaling the 950° parameter set.

2.3 The initial model

We start with a standard Chaboche [10–13] model for this calibration at $T = 950^\circ \text{C}$. The following presents the equations in 1D. Extending to 3D requires only replacing the the viscoplastic rate equations with its J_2 flow equivalent and updating the backstress evolution equation to use symmetric rank two tensors instead of signed scalars.

The model has a unified viscoplastic form

$$\dot{\sigma} = E (\dot{\varepsilon} - \dot{\varepsilon}_{vp}) \quad (2.2)$$

where E is the Young’s modulus, $\dot{\varepsilon}$ the total mechanical strain rate, here taken from the experimental strain history, and $\dot{\varepsilon}_{vp}$ is the viscoplastic strain rate. This type of model naturally captures plastic-creep interaction at high temperatures without needing to explicitly couple creep and plastic strain models, for example by altering the internal variable evolution equations. The model evolves the isotropic and kinematic hardening, but keeps the flow resistance constant:

$$\dot{\varepsilon}_{vp} = \left\langle \frac{|\sigma - X| - \sigma_0 - K}{\eta} \right\rangle^n \text{sign}(\sigma - X) \quad (2.3)$$

where σ is the stress, X the total kinematic hardening, σ_0 a threshold stress, K the isotropic hardening, η the constant flow resistance, and n the rate sensitivity. The initial model decomposes the kinematic hardening into three backstresses:

$$X = \sum_{i=1}^3 X_i. \quad (2.4)$$

Parameter	Description	Value	Units
E	Young's modulus	136000	MPa
n	Rate sensitivity	5.772	-
η	Drag stress	480.9	MPa
σ_0	Threshold stress	9.623	MPa
R	Isotropic softening stress	-17.73	MPa
δ	Isotropic softening rate	10.32	-
C_1	Backstress 1 hardening rate	643.933	MPa
C_2	Backstress 2 hardening rate	40.32367	MPa
C_3	Backstress 3 softening rate	-20.600	MPa
γ_1	Backstress 1 dynamic recovery	103.7	-
γ_2	Backstress 2 dynamic recovery	5.089	-
γ_3	Backstress 3 dynamic recovery	0.9823	-

Table 2.2: Calibrated parameters for the initial model at 950° C.

Each backstress evolves per the standard Chaboche model

$$\dot{X}_i = \frac{2}{3} C_i \dot{\epsilon}_{vp} - \gamma_i X_i |\dot{\epsilon}_{vp}| \quad (2.5)$$

here C_i and γ_i are the kinematic hardening and dynamic recovery parameters. Finally, the model includes Voce isotropic hardening

$$\dot{K} = \delta (R - K) |\dot{\epsilon}_{vp}|. \quad (2.6)$$

The L-BFGS optimization method described in Section 2.1 produces the calibrated properties in Table 2.2. The optimization scheme fit all parameters except the Young's modulus (E), which we fixed to the value from ASME Alloy 617 Code Case. Given the number of data points in each test and the number of tests of each type (see Table 2.1), the optimization loss function (Eq. 2.1) will bias the calibrated model towards accurately fitting the creep-fatigue and fatigue tests, at the expensive of the creep and tension tests. We expect then to need to tune the parameters further to obtain a model that balances the error between all types of loading conditions.

2.4 Comparison to data

Figures 2.1-2.5 compare the calibrated model to the dataset at 950° C. As the calibration process used this data to define the loss function this comparison is not proper validation of the model. Chapter 4 validates the model against data not used in the initial calibration. These figures then simply illustrate the degree to which the model form we selected can represent the available experimental data.

Figure 2.1 compares the model prediction to two repeated tensile tests from the A617 Code Case database, both performed per ASTM E21. Figure 2.1(a) evaluates the model directly against the experimentally-measured time and strain data. Figure 2.1(b) assumes the experiment proceeded at a constant strain rate of $8.33 \times 10^{-5} \text{ s}^{-1}$, which is the E21

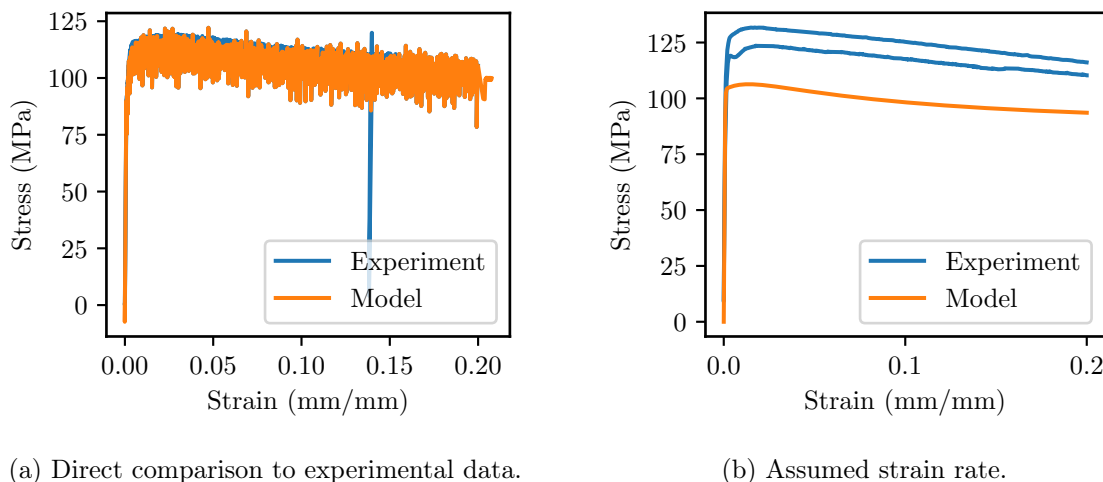


Figure 2.1: Comparison between model predictions and tension test results at 950° C. (a) Raw comparison to experimental data; (b) comparison assuming a constant strain rate of $8.33 \times 10^{-5} \text{ s}^{-1}$.

requirement for the strain rate controlled portion of the test. ASTM E21 allows a switch to stroke control after yield, which means the strain rate will vary after the yield point.

These comparison shows that the model accurately captures the experimental tension test data. It also demonstrates:

1. The need to use the direct experimental test data, rather than abstracted test data. For example, reports of tensile tests often only include the flow curve. This leaves out the time data (i.e. the time corresponding to each strain/stress point). This in effect removes the instantaneous strain rate data required to accurately simulate the experiment.
2. Raw experimental data, particularly at high temperatures, is very noisy. Smoothing the data, as is commonly done for plotting, may remove valuable information, for example small changes in the instantaneous strain rate.

Figure 2.2 then compares the model predictions to the four available creep tests. The initial (primary) creep rates match reasonably between the model and the experimental data. The model form considered in this chapter does not have a mechanism to capture the acceleration in the creep rate during tertiary creep. Chapter 3 addresses this deficiency by altering the form of the model.

Finally, Figures 2.3-2.5 compare the model to the fatigue and creep-fatigue test data. All these tests are fully-reversed, strain-controlled cyclic tests at a strain rate of 10^{-4} s^{-1} some with tensile holds (creep-fatigues) and other test with no holds (pure fatigue). The figure groups the tests by strain range. The code case database contain multiple repeats of each test condition. These figures only show one trial for each test condition. The repeated tests are consistent with the trials shown here.

The model predictions for the fatigue and creep-fatigue tests are excellent. The relatively small errors are predominantly in the initial flow stress on the first half loading cycle,

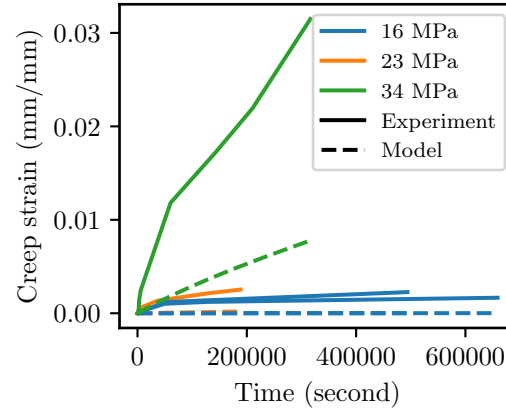


Figure 2.2: Comparison between the model and the available creep data (full creep curves) at 950° C.

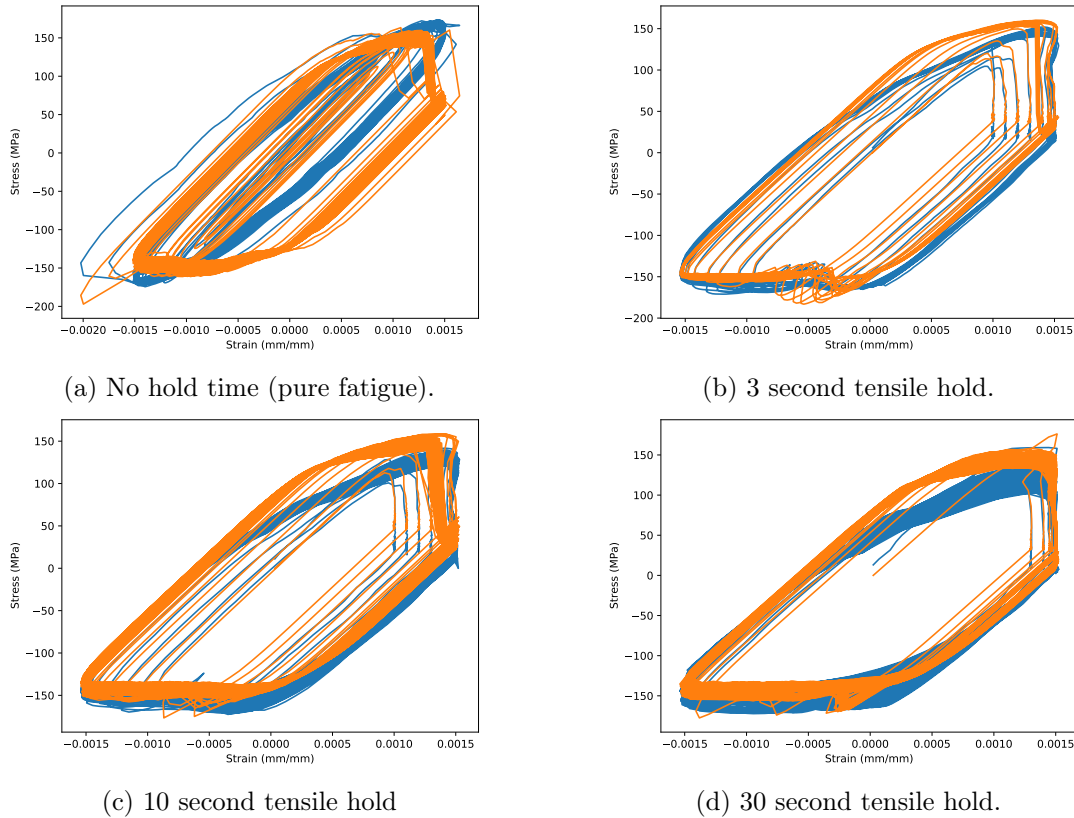
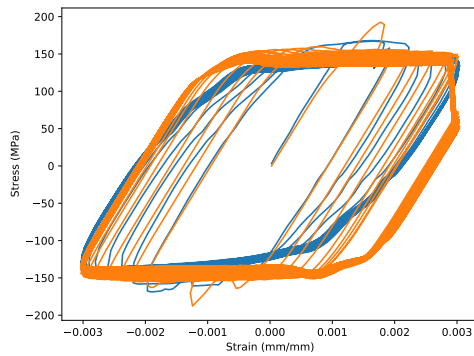
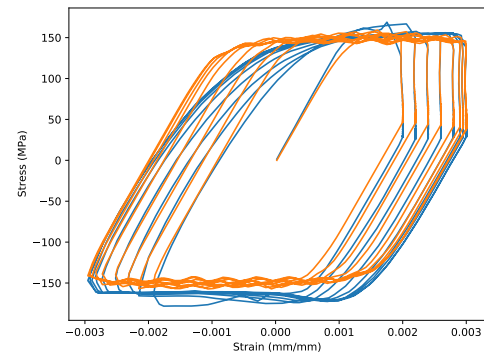


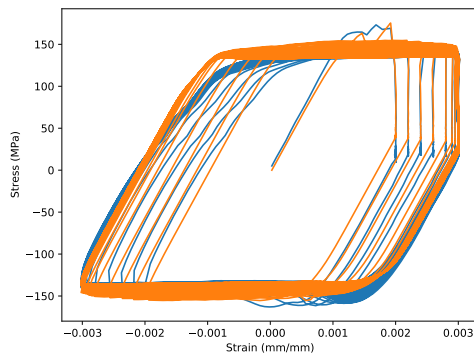
Figure 2.3: Comparison between the test results and the model predictions for the fatigue and creep-fatigue tests at 950° C with $\Delta\epsilon = 0.3\%$. The subcaptions indicate the hold time for each test. The experimental data is blue, the model predictions orange.



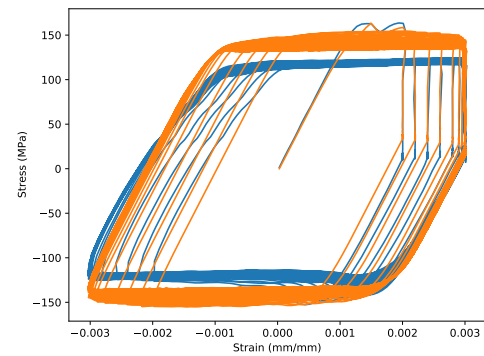
(a) No hold time (pure fatigue).



(b) 3 second tensile hold.

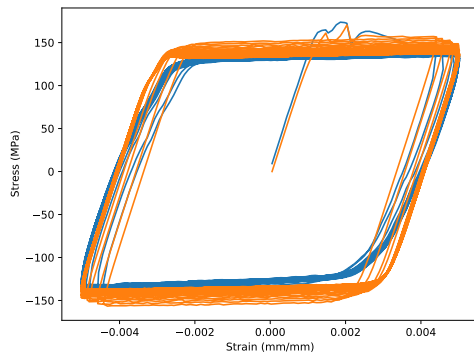


(c) 10 second tensile hold

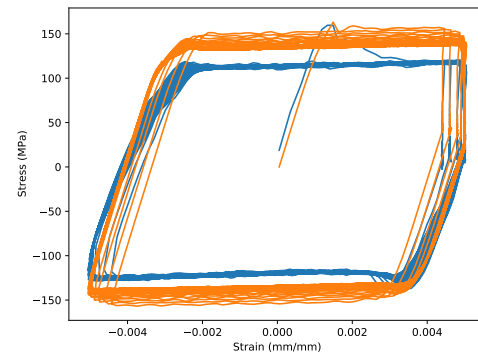


(d) 30 second tensile hold.

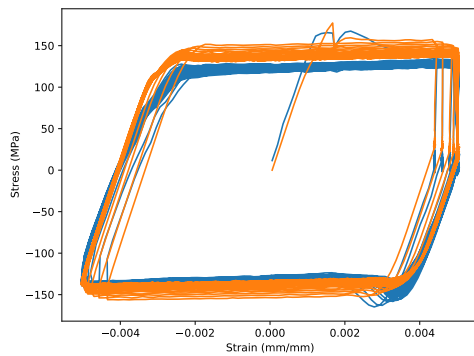
Figure 2.4: Comparison between the test results and the model predictions for the fatigue and creep-fatigue tests at 950° C with $\Delta\varepsilon = 0.6\%$. The subcaptions indicate the hold time for each test. The experimental data is blue, the model predictions orange.



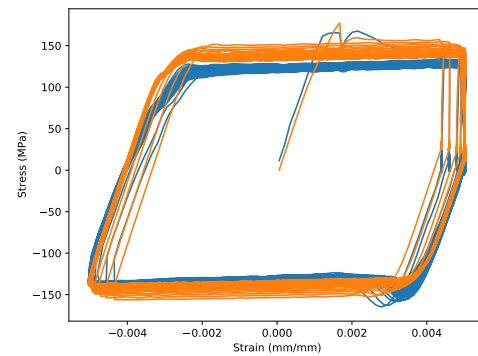
(a) No hold time (pure fatigue).



(b) 3 second tensile hold.



(c) 10 second tensile hold



(d) 30 second tensile hold.

Figure 2.5: Comparison between the test results and the model predictions for the fatigue and creep-fatigue tests at 950° C with $\Delta\epsilon = 1.0\%$. The subcaptions indicate the hold time for each test. The experimental data is blue, the model predictions orange.

propagated through subsequent cyclic behavior, with the model accurately capturing the subsequent kinematic hardening. Note that the flow stress on the first half cycle does not depend on the test strain range or test hold time (as the hold has not occurred yet). As such, the variation in the experimentally-measured flow stress on the first half cycle between the different tests with different hold times in Figure 2.5 cannot be explained by the experimental conditions. Moreover, these tests are all from samples machined from the same heat of material. Therefore, the test-to-test differences in the initial flow stress must be random experimental variation. This is common for very high temperature tests, like these tests at 950° C, where there is considerable compliance in the load train and test measurement equipment. The deterministic model cannot account for this random error and so the best approach is the one adopted here: fit the model to the average of several measurements.

Except for these few discrepancies in the initial flow stress, the model accurately predicts the cyclic stress-strain hysteresis in the samples, including the effect of the tension holds. The model even successfully captures some of the complex details of the experimental response, for example the initial overshoot in the flow stress on the first cycle. Apparently this is not entirely caused by a material effect but rather difficulty in controlling the strain rate at the onset of yielding, likely again due to the high test temperature. Given the heat-to-heat variation in material properties and the level of accuracy needed for a model when applying the ASME design by inelastic analysis rules, this comparison suggests the 950° C model has sufficient accuracy for inclusion in the Appendix Z. However, this calibration approach can only be applied to the 950° C data, as we do not have complete records of the experiments for most of the lower temperature data.

3 Temperature scaling: extending the model to the full temperature range

3.1 Available data

Compared to the data available at 950° C the database of experimental results for all another temperature is substantially smaller. Table 3.1 describes the Alloy 617 test data available for calibrating the model. This table lists only standard, uniaxial test data. In addition to these standard test results there is a larger collection of abstracted test data — descriptions of tests that do not include the full time, strain, stress information — and several non-standard test results that we use to validate the model in Chapter 4.

For the most part this additional test data comes from either the original Code Case test campaign or from tests conducted through the ART program to support the model development. While the database does sample the critical temperature range, spanning from room temperature to the ASME maximum use temperature, it is not sufficient to calibrate unique Chaboche model parameters over the entire range. Specifically, we do not have a significant database of creep-fatigue test results for temperatures other than 950° C. This means we cannot repeat the calibration process described in Chapter 2 to cover the rest of the temperature range.

3.2 Scaling parameters

Instead, we elected to scale the model parameters calibrated at 950°C to account for the temperature dependence in the material rate sensitivity, initial flow stress, and hardening response. This is the same approach adopted by Sham et al. [9] in the original Alloy 617 model developed based on the Code Case data. Sham, Walker, and coworkers were confronted with the same problem — the lack of data at lower temperatures. While our previous work does not support the use of this model directly in the new Appendix Z [8], the temperature scaling approach allows us to overcome the lack of data and develop a reasonably accurate model over the entire Alloy 617 use range. We adopt several different strategies to scale/calibrate different parts of the model to lower temperatures.

Test type	Conditions	Sources
Standard tension	20°, 300°, 400°, 650°, 700°, 750°, 800°, 850°, and 900° C	A617 CC
Creep	Different stresses, including repeated tests, from 750° to 1000° C	A617 CC and[17]
Strain controlled-cyclic	Standard fatigue ($R = -1$, no holds) at 20°, 200°, 400°, 600°, 850°, and 900°	A617 CC, dedicated tests

Table 3.1: Standard experimental data for temperatures other than 950° C. Records labeled “A617 CC” are from the Alloy 617 ASME Code Case qualification effort. Records labeled “dedicated tests” are from a test campaign through the ART program specifically for calibrating the model discussed here.

Temperature (°C)	Modulus (GPa)
25	201
100	196
200	191
300	187
400	181
500	174
600	167
700	160
800	152
900	141
950	136
983	134

Table 3.2: The temperature-dependent Young’s modulus of Alloy 617, per the ASME Code Case.

Several of these scaling relations relate material properties to the temperature dependent value of the material shear modulus, μ . We calculate the shear modulus using the Alloy 617 Code Case values of the Young’s modulus, reproduced in Table 3.2, the ASME value of the Poisson’s ratio for Alloy 617, $\nu = 0.31$, and the following equation:

$$\mu = \frac{E}{2(1 + \nu)}. \quad (3.1)$$

3.2.1 Rate sensitivity and initial flow stress

We use an approach based on the Kocks-Mecking theory [18, 19] developed by the author and others [20] to scale the model’s initial flow stress and rate sensitivity to match experimental data. The input to this process are the tensile stress data, specifically the measured yield stress, and the creep test data, specifically the initial primary creep rate. The approach takes the temperature, strain rate, and flow stress information from these tests and plots it on a normalized Kocks-Mecking diagram where the x-axis is the normalized activation energy

$$g = \frac{kT}{\mu b^3} \log \frac{\dot{\epsilon}_0}{\dot{\epsilon}} \quad (3.2)$$

with T the absolute temperature, k the Boltzmann constant, b the material Burgers vector length, $\dot{\epsilon}_0$ a reference strain rate, and $\dot{\epsilon}$ the characteristic test strain rate and the y-axis is the log of the flow stress, normalized by the material’s temperature dependent shear modulus

$$f = \frac{\sigma_f}{\mu}. \quad (3.3)$$

For Alloy 617 we use $b = 24.8 \text{ nm}$ and $\dot{\epsilon}_0 = 10^{10} \text{ s}^{-1}$.

Figure 3.1 shows this diagram for Alloy 617, using the data described in Table 3.1. For most materials, including Alloy 617, a bilinear model fits the data. One branch of the bilinear

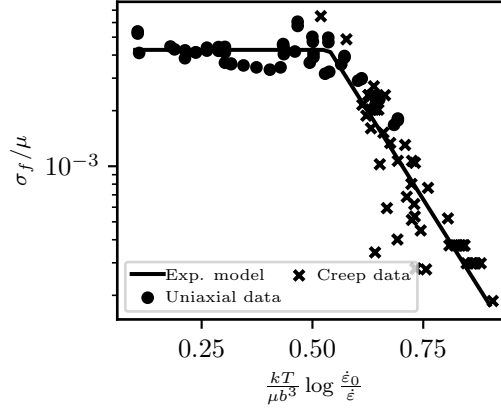


Figure 3.1: Kocks-Mecking diagram for Alloy 617.

Parameter	Value
A	-7.985
B	-0.6696
C	-5.550
g_0	0.6112

Table 3.3: Kocks-Mecking parameters used in the final model. Parameters are all non-dimensional.

model has zero slope, which means the flow stress does not depend on the strain rate. On this branch therefore the material response is rate independent, with a yield stress given by

$$\sigma_y = \mu e^{C_{km}} \quad (3.4)$$

where C_{km} is the y-coordinate of the horizontal line on the semi-log plot. In the second region, a linear slope on the semi-log implies a power law viscoplastic model with

$$n = \frac{-\mu b^3}{kT A_{km}} \quad (3.5)$$

and

$$\eta = e^{B_{km}} \mu \dot{\epsilon}_0^{-1/n} \quad (3.6)$$

where A_{km} is the slope of the linear branch and B_{km} the intercept. So given a bilinear Kocks-Mecking diagram characterized by A_{km}, B_{km}, C_{km} and g_0 , the intersection point between the constant and linear slope regions, we can fully characterize the material rate sensitivity and initial flow stress.

Table 3.3 provides the Kocks-Mecking parameters used to scale the model rate sensitivity and initial flow stress. These are tuned slightly from our original paper [20], accounting for the additional data available here to calibrate the model in between room temperature and 750° C, not available for the original work.

The final model, described in Chapter 4, includes a mechanism for switching between a rate dependent and a rate independent response based on the Kocks-Mecking theory and

these calibrated parameters. The model then accounts for the full rate sensitivity of the material, spanning from room temperature to the maximum ASME use temperature and all realistic component loading strain rates.

3.2.2 Isotropic and kinematic hardening

Separating and calibrating the material isotropic and kinematic hardening requires an extensive database of cyclic tests, like the database available for 950° C. As we do not have that type of data for the lower temperatures instead we adopt Walker's procedure and keep the Chaboche parameters describing the material kinematic hardening fixed to the 950° C values and scale only the isotropic hardening to account for the material temperature dependence. We then have the dedicated, ART Program fatigue test data available to ensure that this approach reasonably accounts for the material cyclic hardening at lower temperatures.

For Alloy 617 there are two distinct regions of work hardening. Above about 800° C the material starts as perfectly plastic, with no significant work hardening, and shifts towards work softening as the temperature increases. Below 750° C the material hardens significantly. A change in the precipitation kinetics of the γ' phase causes this shift in behavior. In both regions we can use a Voce hardening model of the form described in Chapter 2 to describe the material behavior. The model can be characterized by two parameters: the saturated work hardening R (the difference between the material yield strength and the tensile strength) and the initial rate of work hardening θ_0 . Chapter 2 uses the parameter δ (along with R) to describe the Voce model instead. This parameter can be written as a function of R and θ_0

$$\delta = \frac{\theta_0}{R} \quad (3.7)$$

In the region below 750° C we calibrate the material isotropic hardening to match the experimentally-measured average difference between the material yield stress and the material tensile strength. We represent the average yield stress of Alloy 617 by $1.25S_y$, with S_y the ASME material yield strength, as tabulated in the Alloy 617 Code Case. We represent the material ultimate tensile strength by the ASME tensile strength S_u . The 1.25 in the yield strength equation approximately scales the ASME strength to the nominal, average value. Figure 3.2 plots this difference as a function of temperature along with a second-order polynomial fit to the curve, used to specify the amount of hardening in the model. However, the model combines isotropic and kinematic hardening and so only some fraction of this difference can be attributed to isotropic hardening. We calibrated this fraction by matching the tensile curves (as the kinematic hardening is fixed), keeping a constant, fixed fraction for all temperatures. The calibrated fraction is 0.70.

We keep the initial hardening slope in the low temperature region fixed to

$$\delta = \frac{0.04\mu}{R}. \quad (3.8)$$

This value accurately represents the initial hardening slope when simulating the available tensile data.

In the high temperature regime we calibrate the model by transitioning from $R = 0$ at 800° C to $R = -17.73$ MPa (the calibrated value from the Chapter 2 model) at 950° C. The

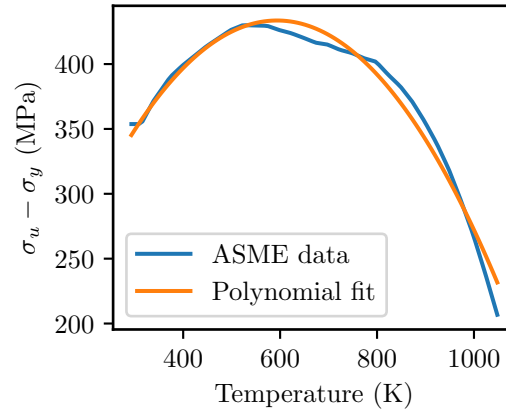


Figure 3.2: Difference between S_u and $1.25S_y$ as a function of temperature.

model is not sensitive to the value of δ in this regime where there is slight work softening and so we keep that parameter fixed to $\delta = 10.32$, again the calibrated value of the Chapter 2 model.

This only leaves the transition between the two regimes in the $750^\circ \leq T \leq 800^\circ \text{ C}$ range. We simply linearly interpolate between the parameter values at 750° and 800° C to complete the model. The following equations then describe the complete Voce model as a function of temperature:

$$R = \begin{cases} 0.70 \left(-9.778 \times 10^{-4} (T + 273.15)^2 + 1.161 (T + 273.15) + 88.93 \right) & T < 750^\circ \text{ C} \\ -3.546 ((T + 273.15) - 1023.15) + 177.3 & 750^\circ \text{ C} \leq T < 800^\circ \text{ C} \\ -0.1182 ((T + 273.15) - 1073.15) & 800^\circ \text{ C} \leq T < 950^\circ \text{ C} \\ -17.73 & T \geq 950^\circ \text{ C} \end{cases} \quad (3.9)$$

$$\delta = \begin{cases} \frac{0.04\mu}{R} & T < 750^\circ \text{ C} \\ -0.06228188T + 60.145026 & 750^\circ \text{ C} \leq T < 800^\circ \text{ C} \\ 10.32 & T \geq 800^\circ \text{ C} \end{cases} \quad (3.10)$$

The temperature has units of Celsius in these formula.

3.2.3 Tertiary creep: Hayhurst-Leckie damage

The flow stress, rate sensitivity, and hardening provide a complete, temperature-dependent model corresponding to the single temperature model developed in Chapter 2. However, that model did not include a mechanism for capturing the accelerating creep rate during tertiary creep. One option we have used in the past for capturing this effect is to supplement the material deformation model with a creep damage model [6]. Damage models of this type reduce the effective elastic properties of the material by some damage variable ω and provide an evolution equation for that damage variable as a function of time, temperature, and stress. Our past work [6] provides a method for calibrating a Hayhurst-Leckie [21–23]

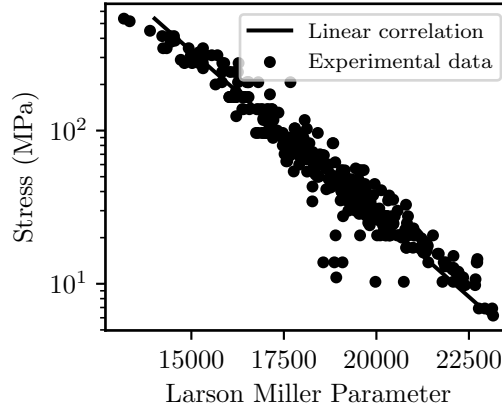


Figure 3.3: Linear Larson-Miller correlation used to fix the damage model parameters.

Parameter	Value
C_{lm}	9.666
A_{lm}	26779
B_{lm}	-4676.9
ϕ	1.8

Table 3.4: Calibrated Larson-Miller parameters and the Hayhurst-Leckie parameter ϕ defining the damage model.

type damage model with the form

$$\dot{\omega} = \frac{1}{(1 - \omega)^\phi} \left(\frac{\sigma}{\sigma_0} \right)^\xi \quad (3.11)$$

against creep rupture data, described with a linear Larson-Miller relation. Specifically, the linear Larson-Miller relation of the form

$$(T + 273.15) (\log_{10} t_R + C_{lm}) = A_{lm} + B_{lm} \log_{10} \sigma \quad (3.12)$$

fixes the values of two of the three configurable parameters in the Hayhurst-Leckie damage model:

$$\xi = -\frac{B_{lm}}{T + 273.15} \quad (3.13)$$

$$\sigma_0 = \frac{10^{C_{lm}(T+273.15)/B_{lm} - A_{lm}/B_{lm}}}{(\phi + 1)^{(T+273.15)/B_{lm}}}. \quad (3.14)$$

The remaining parameter, ϕ , can be tuned to match the shape of the full creep curve data.

Figure 3.3 shows a linear Larson-Miller correlation between the Alloy 617 rupture data collected as part of the Code Case qualification effort. Table 3.4 lists the values of A_{lm} , B_{lm} , and C_{lm} , along with the best-fit value of ϕ , resulting from the Larson-Miller correlation and the calibration against the full creep curves listed in Table 3.1.

3.3 Verifying the scaled models

The following subsections compares the experimental data described in Table 3.1 to the model predictions, using the temperature scaling strategies described above. For the most part these comparisons cannot be considered model validation, as the test data was used to fit parts of the temperature-scaling methods detailed above. However, the comparisons illustrate how adequately the scaled model captures trends in the temperature-dependent behavior of Alloy 617. Moreover, because we scaled the 950° C parameters with simple models, rather than refitting the model at each temperature, these comparisons are partial validation as the calibration approach could not freely change the model parameters to fit the data.

3.3.1 Tensile curves

Figure 3.4 compares the simulated and measured tensile curves. With the exception of 750° to 800° C and 950°C, the simulated tensile curves all closely match at least one experimental curve (for the cases where repeated trials are available) or the single available curve. Section 4.3 discusses the apparent inaccuracy at 950°C. A switch in material deformation mechanism related to the precipitation kinetics of the γ' phase causes inconsistent behavior around 750° to 800° C. Rather than try to capture this complex behavior, the response of the model (transition to perfect plasticity at the average flow stress) adequately captures the response for use with the ASME engineering design rules.

3.3.2 Creep curves

Figure 3.5 compares the model predictions to the experimental creep curves. The model captures the average trend (for repeated conditions) in the experimental creep rate. In particular, the model captures the transition to tertiary creep accurately as well as the average creep strain/time relation at higher strains. Chapter 4 further validates the model against experimental primary creep (time to 1% strain) data.

3.3.3 Fatigue and cyclic hardening

The ART program sponsored a series of fully-reversed standard fatigue tests to support the development of this model. Figure 3.6 compares the model to the experimental results by plotting the experimental and measured maximum and minimum stress as a function of cycle count. These cyclic hardening curves provide a check on the balance of isotropic versus kinematic hardening embedded in the model

There are some discrepancies between the initial flow stress for the new ART material versus the A617 Code Case tension tests used to set the initial yield stress in Section 3.2. Section 4.3 discusses the reasons for this discrepancy and demonstrates that the error between the model and the new experiments is acceptable, given the heat-to-heat variation expected for Alloy 617. However, to correct for the flow stress differences the figure plots both the raw cyclic hardening curve and the experimental hardening curve shifted to the initial flow stress predicted by the model.

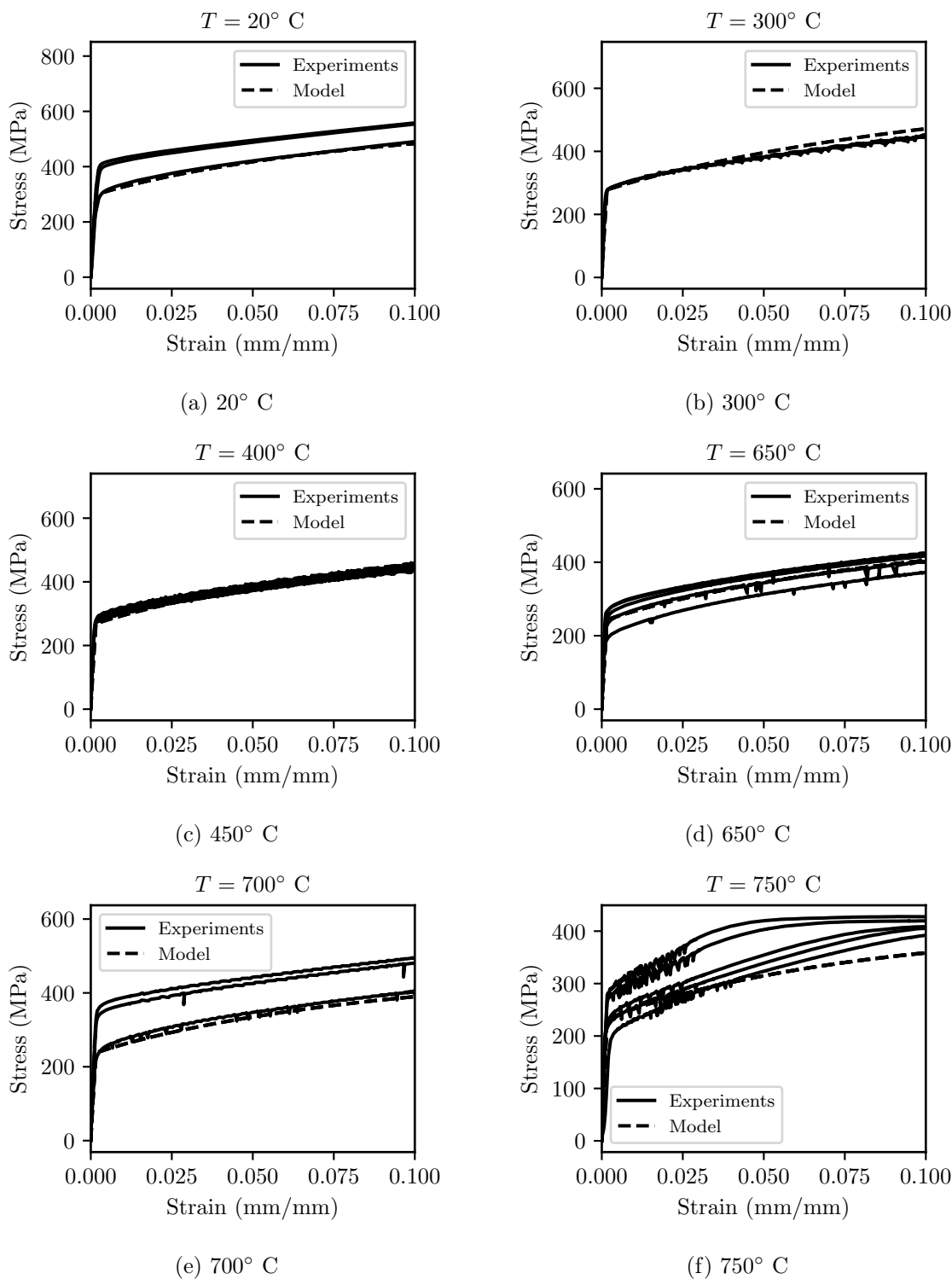


Figure 3.4: Comparison between the simulated and experimental tensile curves.

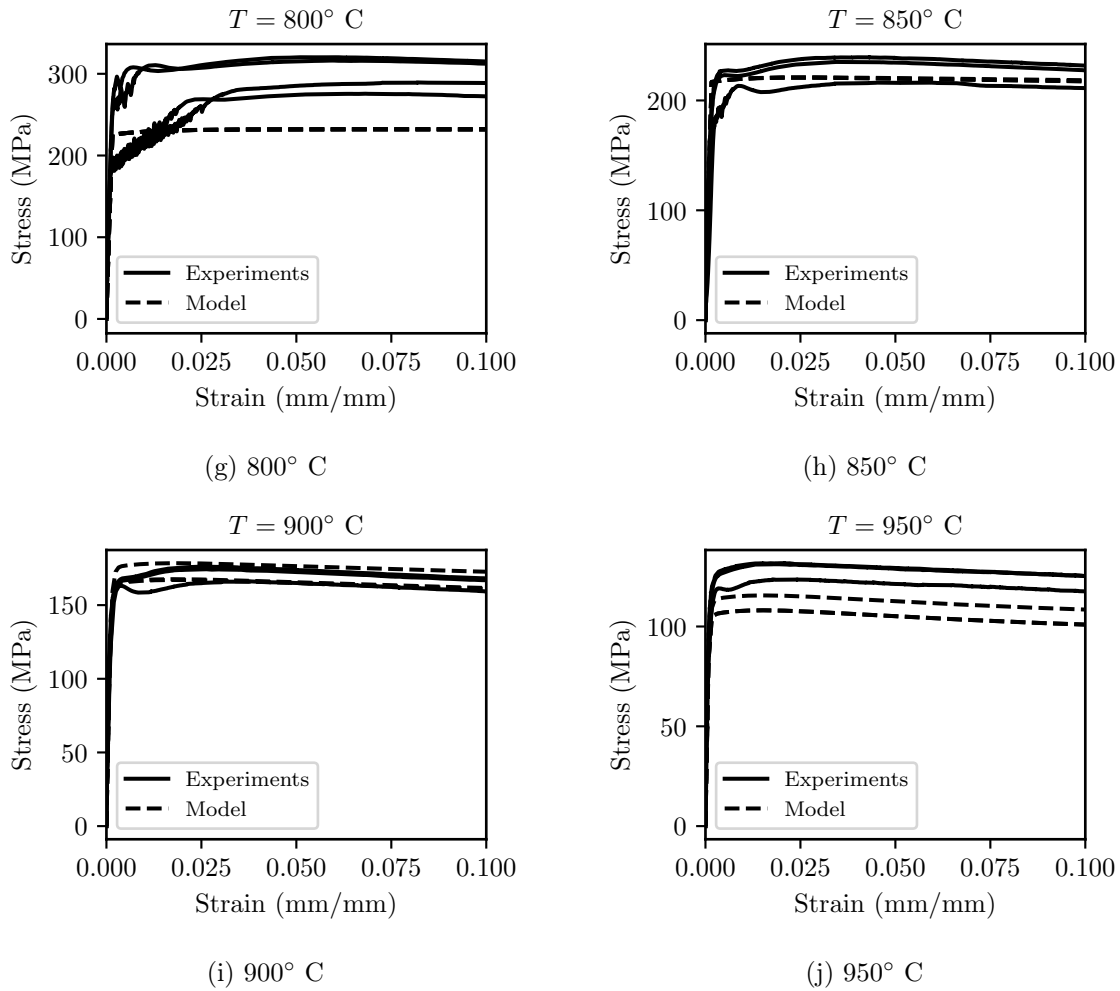
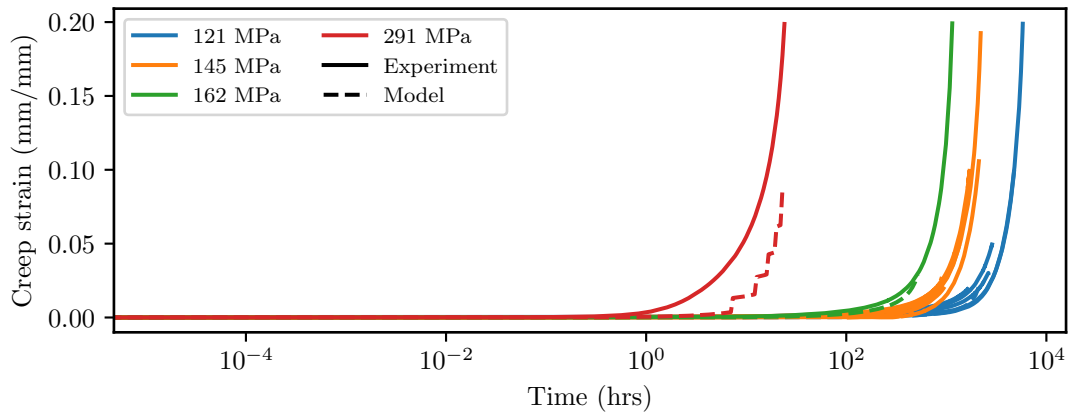
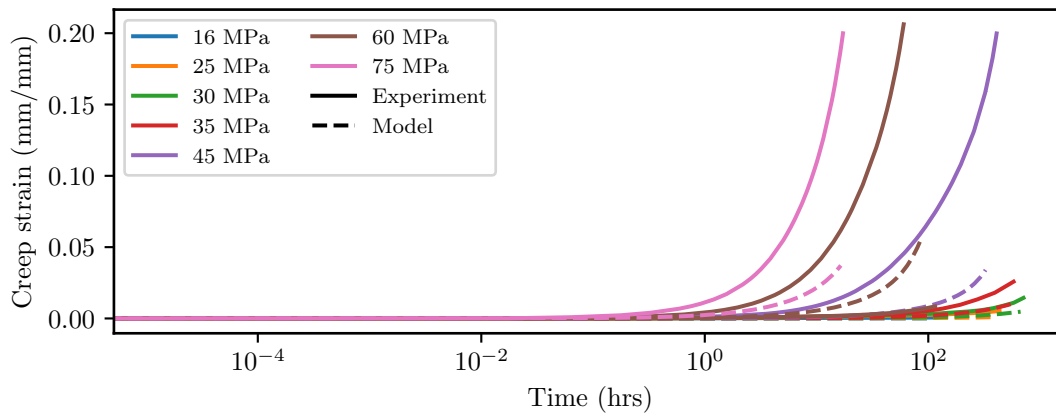


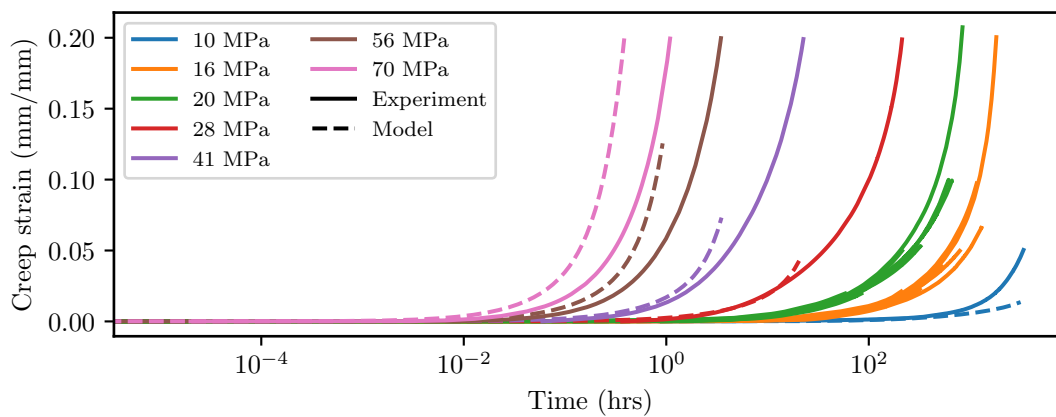
Figure 3.4: Comparison between the simulated and experimental tensile curves (continued).



(a) 750° C



(b) 900° C



(c) 1000° C

Figure 3.5: Comparison between the simulated and experimental creep curves.

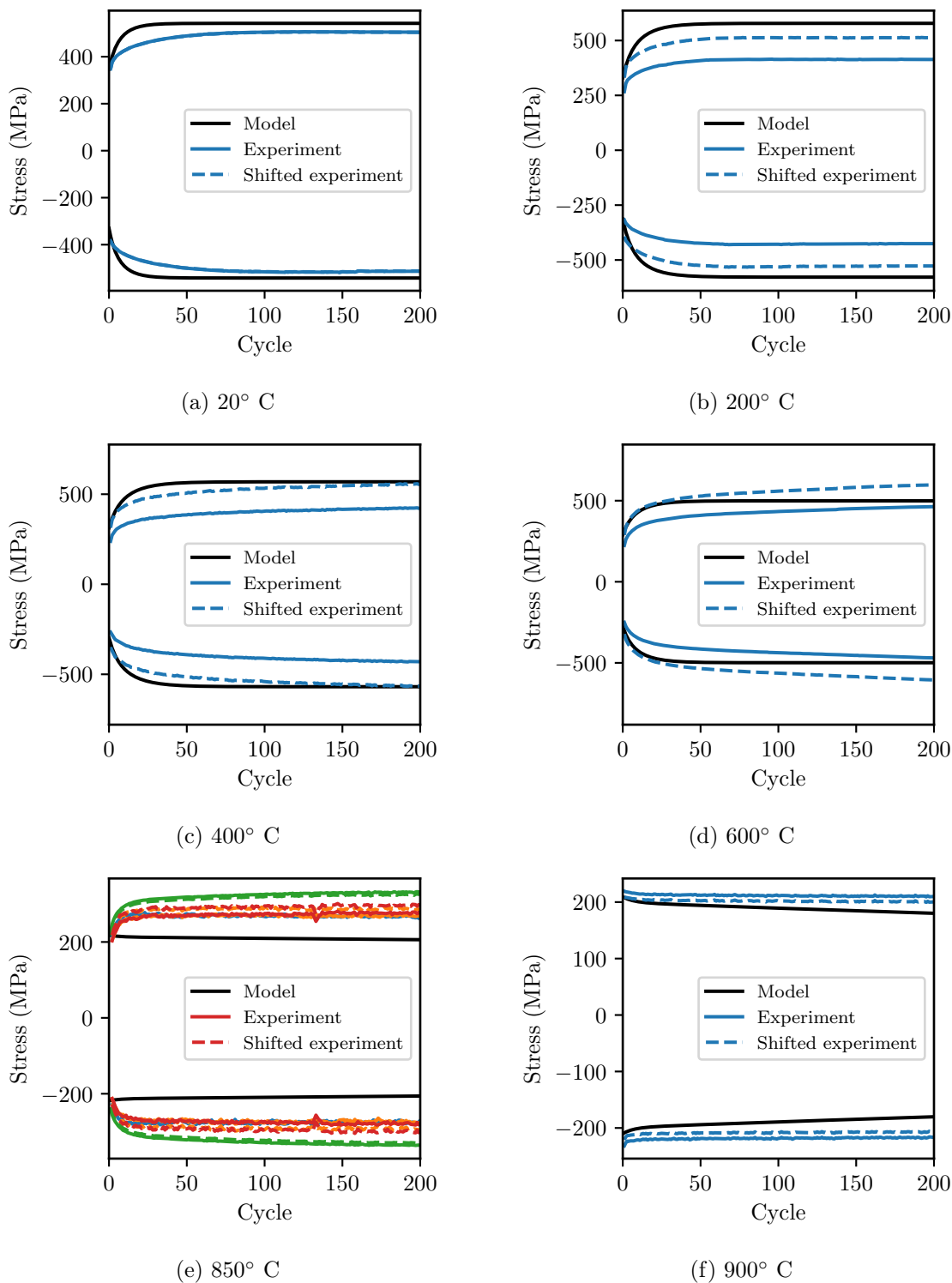


Figure 3.6: Cyclic hardening curves comparing the model to fatigue test at several different temperatures.

With or without the the correction, all the curves match within the expected range of experimental variation except for the 200° C and 400° C tests. These two tests match after accounting for the discrepancy in the initial flow stress. The model's cyclic hardening response could likely be improved if additional fatigue and creep-fatigue data was available by better balancing/calibrating the Chaboche kinematic hardening. However, even this level of accuracy is sufficient for engineering design with the Section III, Division 5 rules.

3.3.4 Cyclic hysteresis at 950° C

This final check compares the detailed cyclic response of the model and experiments at 950° C by plotting the predicted and actual stress/strain hysteresis loops for fully-reversed, strain controlled fatigue and creep-fatigue for a 1% strain range. This comparison duplicates information in Figures 2.3-2.5. It simply serves to check that the alterations made to the model by introducing the temperature scaling do not significantly affect the accuracy of the original model at 950° C. The comparison demonstrates the model continues to accurately reproduce the cyclic response of the material at 950° C.

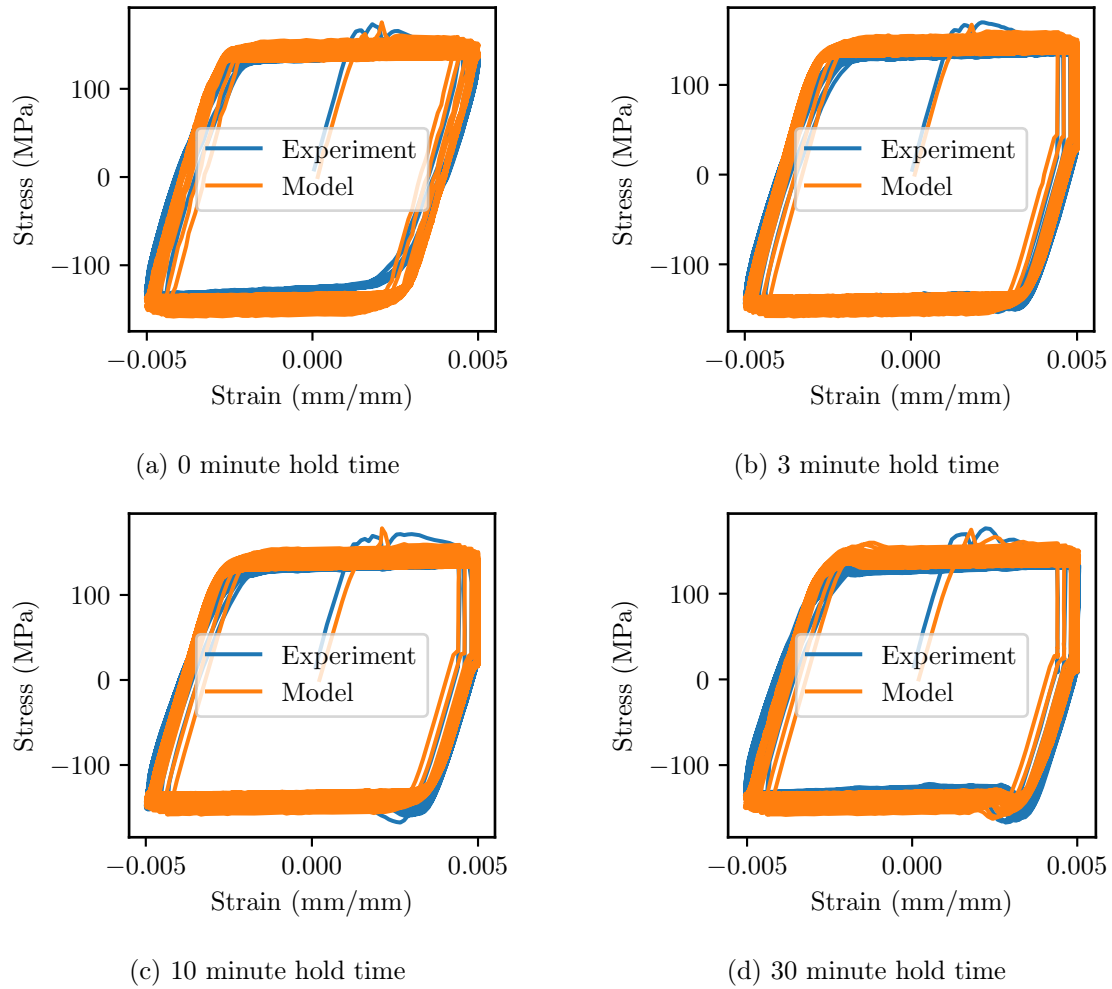


Figure 3.7: Reassessment of the model versus the 950° C creep-fatigue data.

4 Validation comparisons

4.1 The final model

The following equations together with Table 4.1 describe the model in the full 3D form. These equations, and the corresponding table, will form the core of the ASME Code change proposal adding the Alloy 617 model to Appendix Z.

4.1.1 Rate equations

Four rate equations define the complete model

$$\dot{\boldsymbol{\sigma}} = (1 - \omega) \mathbf{C} : \left(\dot{\boldsymbol{\varepsilon}} - \dot{\gamma} \frac{\partial f}{\partial \boldsymbol{\sigma}} - \alpha \dot{T} \mathbf{I} \right) \quad (4.1)$$

with \mathbf{C} the isotropic elasticity tensor, defined by the Young's modulus E and Poisson's ratio ν , $\dot{\boldsymbol{\varepsilon}}$ the total strain rate, $\dot{\gamma}$ the consistency parameter, and $\frac{\partial f}{\partial \boldsymbol{\sigma}}$ the flow direction, both defined below, α the temperature-dependent instantaneous coefficient of thermal expansion, \dot{T} the temperature rate, and \mathbf{I} the identity tensor.

$$\dot{K} = \delta (R - K) \dot{\gamma} \quad (4.2)$$

the isotropic hardening rate, with δ and R parameters, and $\dot{\gamma}$ the consistency parameter, defined below.

$$\dot{\mathbf{X}}_i = \left(\frac{2}{3} C_i \frac{\partial f}{\partial \boldsymbol{\sigma}} - \sqrt{\frac{2}{3}} \gamma_i \mathbf{X}_i \right) \dot{\gamma}, \quad i \in [1, 3] \quad (4.3)$$

the backstress evolution equation, with C_i and γ_i parameters. Finally, the damage rate is

$$\dot{\omega} = \frac{1}{(1 - \omega)^\phi} \left(\frac{\sigma_{vm}}{\sigma_0} \right)^\xi \quad (4.4)$$

with ϕ , ξ , and σ_0 all parameters and σ_{vm} the von Mises stress.

The consistency parameter $\dot{\gamma}$ switches between a rate independent and rate dependent response based on the normalized activation energy:

$$g = \frac{kT}{\mu b^3} \log \frac{\dot{\varepsilon}_0}{\sqrt{2/3} \dot{\boldsymbol{\varepsilon}} : \dot{\boldsymbol{\varepsilon}}} \quad (4.5)$$

$$\dot{\gamma} = \begin{cases} \dot{\gamma}_{ri} & g \leq g_0 \\ \dot{\gamma}_{rd} & g > g_0 \end{cases} \quad (4.6)$$

For both cases the flow direction and the consistency parameter are defined in terms of the flow function, which uses standard J_2 /von Mises flow theory

$$f = \sqrt{\frac{3}{2} (\mathbf{s} - \mathbf{X}) : (\mathbf{s} - \mathbf{X})} - (\sigma_0 + K) \quad (4.7)$$

with \mathbf{X} the total backstress

$$\mathbf{X} = \sum_{i=1}^3 \mathbf{X}_i \quad (4.8)$$

\mathbf{s} the stress deviator

$$\mathbf{s} = \boldsymbol{\sigma} - \frac{1}{3} \text{tr}(\boldsymbol{\sigma}) \mathbf{I} \quad (4.9)$$

where $\boldsymbol{\sigma}$ is the stress and

$$\sigma_0 = \begin{cases} \sigma_y & g \leq g_0 \\ 0 & g > g_0 \end{cases} \quad (4.10)$$

depends on the normalized activation energy. The consistency parameter in the rate independent regime is given by the standard rate independent flow theory defined by the Kuhn-Tucker conditions:

$$\dot{\gamma}_{ri} > 0 \quad (4.11)$$

$$f \leq 0 \quad (4.12)$$

$$\dot{\gamma}_{ri} f = 0 \quad (4.13)$$

$$\dot{\gamma}_{ri} \dot{f} = 0. \quad (4.14)$$

In the rate dependent regime the consistency parameter is given by

$$\dot{\gamma}_{rd} = \frac{\langle f \rangle^n}{\eta} \quad (4.15)$$

with n and η parameters and $\langle \rangle$ the Macaulay brackets.

4.1.2 Model parameters

The following equation and Table 4.1 define the model parameters. The units are consistent with MPa for stress, °C for temperature, and seconds for time.

4.1.2.1 Rate sensitivity and initial flow stress

$$\mu = \frac{E}{2(1 + \nu)} \quad (4.16)$$

$$\sigma_y = \mu e^{C_{km}} \quad (4.17)$$

$$n = \frac{-\mu b^3}{k(T + 273.15) A_{km}} \quad (4.18)$$

$$\eta = e^{B_{km}} \mu \dot{\epsilon}_0^{-1/n} \quad (4.19)$$

4.1.2.2 Damage model

$$\xi = -\frac{B_{lm}}{T + 273.15} \quad (4.20)$$

$$\sigma_0 = \frac{10^{C_{lm}(T+273.15)/B_{lm}-A_{lm}/B_{lm}}}{(\phi + 1)^{(T+273.15)/B_{lm}}}. \quad (4.21)$$

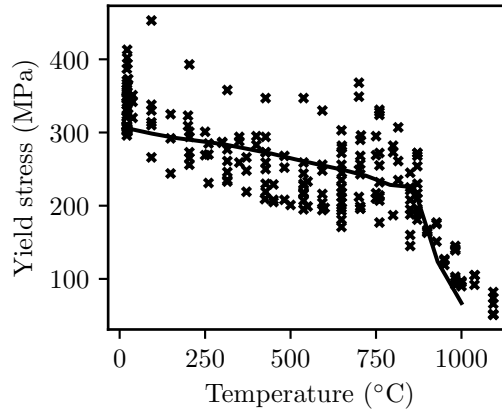


Figure 4.1: Comparison between experimental yield strength measurements and the model prediction as a function of temperature.

4.1.2.3 Isotropic hardening

$$R = \begin{cases} 0.70 (-9.778 \times 10^{-4} (T + 273.15)^2 + 1.161 (T + 273.15) + 88.93) & T < 750^\circ \text{C} \\ -3.546 ((T + 273.15) - 1023.15) + 177.3 & 750^\circ \text{C} \leq T < 800^\circ \text{C} \\ -0.1182 ((T + 273.15) - 1073.15) & 800^\circ \text{C} \leq T < 950^\circ \text{C} \\ -17.73 & T \geq 950^\circ \text{C} \end{cases} \quad (4.22)$$

$$\delta = \begin{cases} \frac{0.04\mu}{R} & T < 750^\circ \text{C} \\ -0.06228188T + 60.145026 & 750^\circ \text{C} \leq T < 800^\circ \text{C} \\ 10.32 & T \geq 800^\circ \text{C} \end{cases} \quad (4.23)$$

4.2 Validation tests

4.2.1 Comparison to abstracted test data

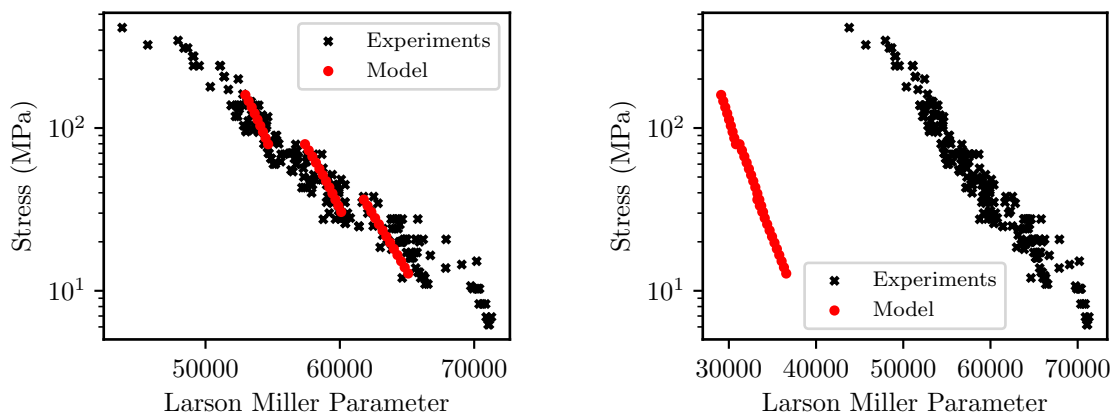
The vast majority of the data collected for the Alloy 617 qualification effort was not full records of experimental tests but rather abstracted test results. For example, the Code Case qualification effort collected hundreds of data points for the material yield strength, creep rupture strength, and time to 1% strain. Chapter 3 used the rupture data to calibrate the model's response in the tertiary creep regime. The calibration process did not use the yield strength and time to 1% strain data, meaning it can serve as a validation test of the final model.

Figure 4.1 compares the yield strength data to the model prediction as a function of temperature. Except for the highest temperatures ($T \geq 950^\circ \text{C}$), the model predictions fall within the experimental scatter, towards the middle of the distribution. We discuss the anomaly in the yield strength at high temperatures in Section 4.3.

A Larson-Miller diagram is one way to summarize time to 1% strain data. Figure 4.2 shows the experimental time to 1% strain data from the Code Case qualification effort,

Symbol	Description	Value
E	Young's modulus	Values in ASME Code Case N-898 (MPa)
ν	Poisson's ratio	Values in ASME Code Case N-898
α	Instantaneous coefficient of thermal expansion	Values in ASME Code Case N-898 (mm/mm/K)
k	Boltzmann constant	1.38064×10^{-20} kJ/K
b	Burgers vector	2.474×10^{-7} mm
A	Kocks-Mecking slope	-7.985
B	Kocks-Mecking intercept	-0.6696
C	Kocks-Mecking horizontal asymptote	-5.550
g_0	Kocks-Mecking intersection point	0.6112
C_m	Larson-Miller parameter	9.666
A_m	Larson-Miller slope	26779
B_m	Larson-Miller intercept	-4676.9
ϕ	Hayhurst-Leckie shape constant	1.8
C_1	Backstress 1 hardening rate	643.933 MPa
C_2	Backstress 2 hardening rate	40.3267 MPa
C_3	Backstress 3 softening rate	-20.600 MPa
γ_1	Backstress 1 dynamic recovery	103.7
γ_2	Backstress 2 dynamic recovery	5.089
γ_3	Backstress 3 dynamic recovery	0.9823

Table 4.1: Model parameters. Units are compatible with megapascals for stress, Celsius for temperature, and seconds for time.



(a) Both experiment and model plotted with the same value of the Larson-Miller parameter C . (b) Experiment and model each plotted with the optimal value of C for that particular dataset.

Figure 4.2: Comparison between the experimental time to 1% strain data and simulated time to 1% data from the viscoplastic model.

summarized on a Larson-Miller plot relating the time to 1% strain and the temperature to the stress. The value of the Larson-Miller parameter, C , in Figure 4.2(a) is that which gives the best log-linear correlation between the experimental data. Figure 4.2(a) also shows simulated time-to-1% data from the model. The simulated points use the same value of C as the experimental data, so the two sets of points are directly comparable.

In Fig. 4.2(a) the model response appears piecewise linear because this Larson-Miller fit forced the model to use the same C parameter as the experimental data. Figure 4.2(b) shows the Larson-Miller correlation for the model data fits better, i.e. appears more linear, for a somewhat different value of C . However, even constrained to the experimental value of C the model data falls within the scatter of the experimental data. This validates the model – it returns a reasonable time to 1% strain for all values of stress and temperature when compared to the experimental database.

4.2.2 ASME isochronous stress-strain curves

In the current ASME Code (i.e. without the new Appendix Z) the isochronous stress-strain curves provide the only information on the deformation response of the Class A materials. For Alloy 617 these isochronous curves are contained in Code Case N-898. Matching these curves suggests that the model reproduces the monotonic (i.e. tension and creep) response the Code assumes for Alloy 617. Our past models for Grade 91 and 316H agreed well with the isochronous curves in the region where actual data is available. The curves (and the model) are extrapolated to lower temperatures, down to the negligible creep range. In this extrapolation range there are differences between the response assumed by the Code and the response assumed by our models.

Ordinarily, comparing the model to these curves is a good validation exercise as the isochronous curves for most of the Class A materials were developed based on a larger, historical, largely unavailable database of experimental results. However, for Alloy 617 the

isochronous curves were developed with the same database of ART tests largely used to establish the initial 950° C parameters for the current model. As such this comparison is not as good of a validation comparison. Despite this, the comparison is still valuable as it affirms that the inelastic model and the current Code isochronous models produce similar responses.

Figures 4.3(a)-(e) plot the Code isochronous curves and the isochronous curves predicted by the model for temperatures from 750° to 950° C. There is little point in comparing the isochronous curves below 700° C as creep is basically negligible and the tensile test comparison in Chapter 3 basically contains all the relevant data. The Code isochronous stress strain concept essentially precludes softening. Instead conventionally models represent a slight softening response as perfectly plastic. The simulated isochronous curves here do the same – where the actual model predicts softening instead these plots show a straight line (i.e. a perfectly plastic response), starting at the strain value where softening initiates. Similarly, the simulated isochronous curves are only generated for steps of 10 MPa, so if the work hardening over 2% strain is less than 10 MPa then the plot shows a straight line

Apart from the initial value of the flow stress at 950° C, the model and the Code ISSCs agree with a reasonable degree of accuracy. Section 4.3 analyzes the difference in the flow stress at 950° C. In particular, the model captures the longer-term creep behavior of the material, as the model and Code ISSC curves converge more accurately for longer times. Additionally, as described in the introduction, the material behavior around 800° C varies greatly both heat-to-heat and test-to-test. The viscoplastic model here attempts to capture the long-term, perfectly plastic flow stress whereas the isochronous curves capture the initial hardening for strains less than 2%. This difference reflects the different uses of the two models: the ISSCs can only be used for strains less than 2.2% whereas the viscoplastic model needs to capture the long term cyclic response of the material, which may include substantial inelastic strain accumulation and cyclic hardening (or softening).

4.2.3 Strain rate jump tests

The ART test campaign supporting the Alloy 617 Code Case development included strain rate jump tests on Alloy 617 at three temperatures, in addition to the more standard tests used to calibrated model, described above. These tests again were not used in calibrating the model and so are used here as a validation assessment. Figure 4.4 compares the model prediction to the experimental jump test data at 750°, 850°, and 950° C. Each jump test followed the same procedure: loading the sample at strain rates of 10^{-6} s^{-1} , 10^{-5} s^{-1} , 10^{-4} s^{-1} , 10^{-3} s^{-1} , and 10^{-2} s^{-1} each for 0.5% strain, in that order.

There are two ways to compare the model and the experiments. The first is whether each jump produced a rate sensitive or insensitive response. In this case the model misses the first rate sensitive jump for the 750° C test but then captures the remaining behavior correctly. The second comparison is between the simulated and experimental flow stress. Here there are some small inconsistencies between the 950° C experiment and model and larger inconsistencies between the model and experiment for 850° C. However, given that the model tensile curve for 850° C is accurate, we attribute this discrepancy to sample variation and the difficulty in consistently controlling the strain rate at high temperatures.

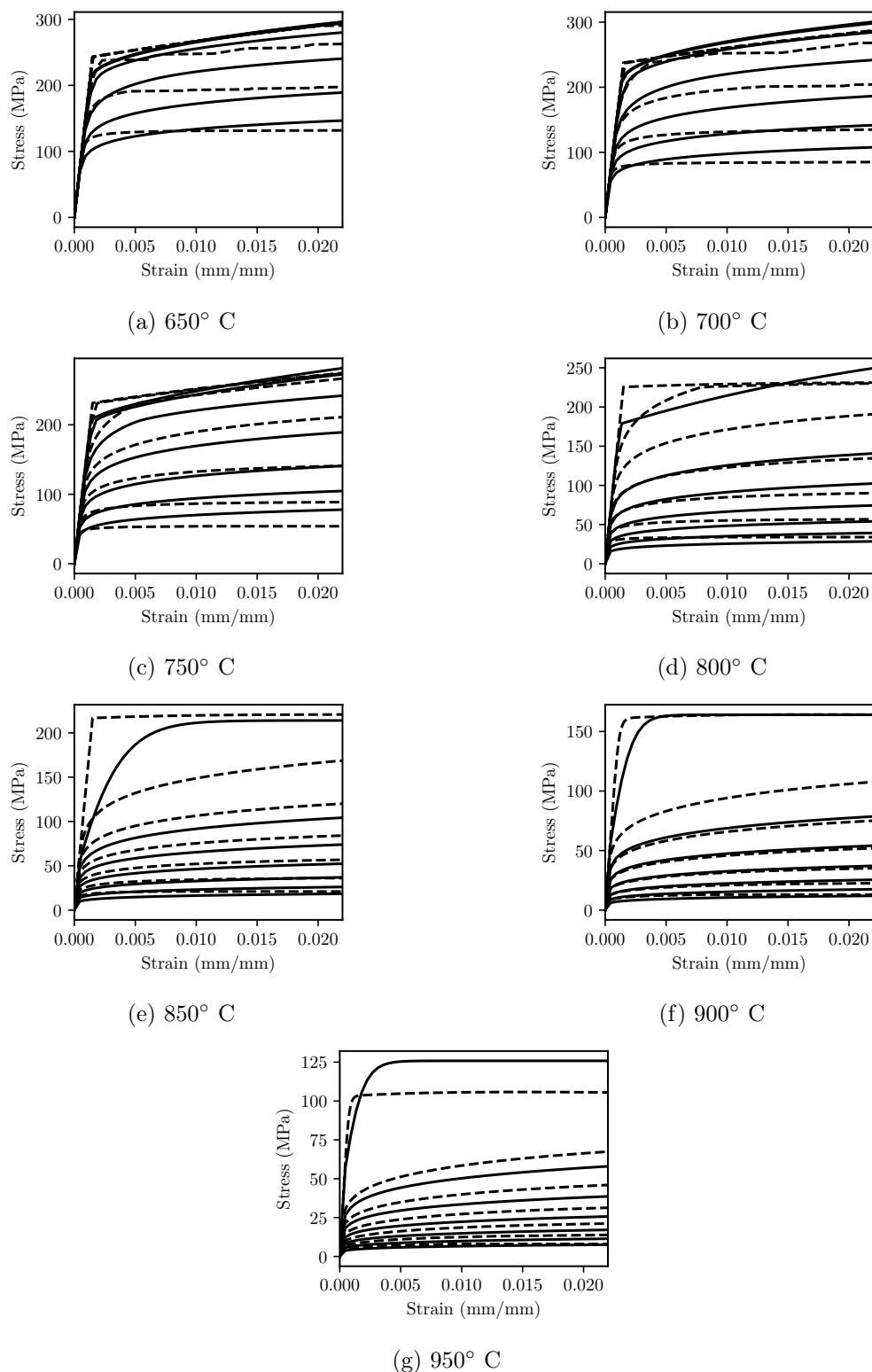


Figure 4.3: Comparison between the Code Case N-898 (solid lines) and the model predicted (dashed lines) isochronous stress-strain curves. The times for the plots, from highest curve to lowest, are 0 hours (hot tensile curve), 1 hour, 10 hours, 1,000 hours, 10,000 hours, and 100,000 hours.

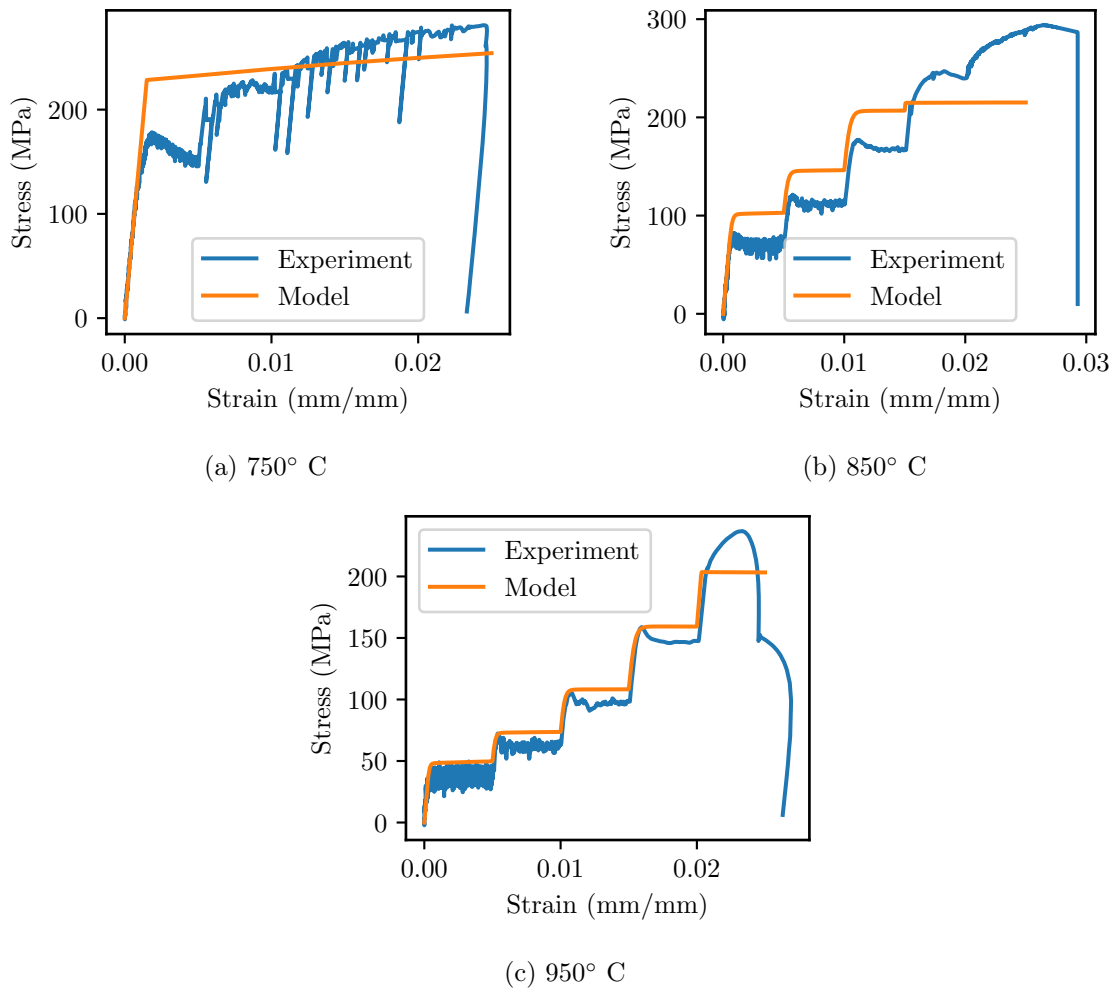


Figure 4.4: Comparison between experimental strain rate jump tests and the model predictions.

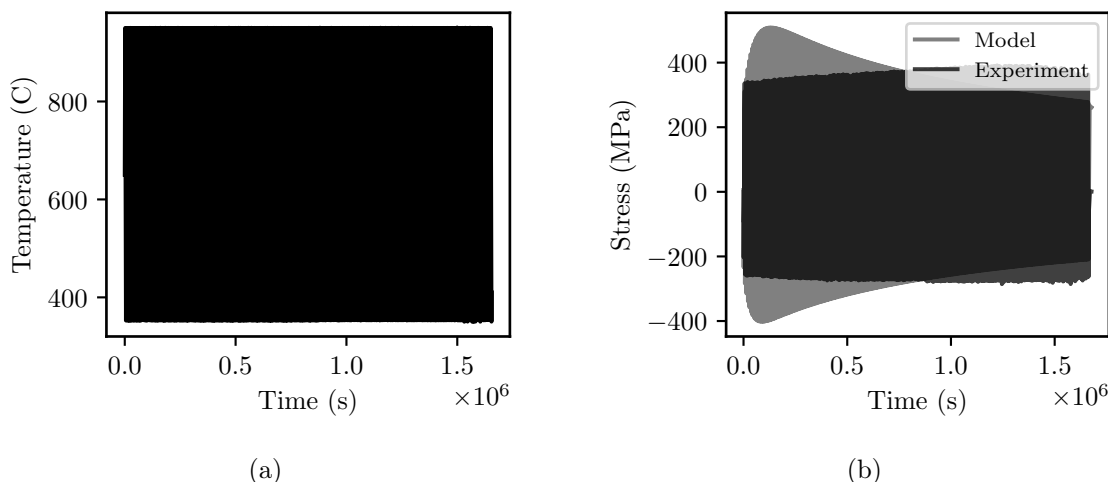


Figure 4.5: Comparison between the thermomechanical experiment and the model predictions. (a) Temperature profile imposed on the sample. (b) Comparison between the model and simulation stress history.

4.2.4 Thermomechanical tests

The current project included a thermomechanical test, specifically for the purpose of validating this inelastic model. The test mechanically restrains a uniaxial test sample (i.e. fixes the total strain to zero) and cycles the sample temperature. This change in temperature imposed a mechanical strain on the material by thermal expansion. These tests are useful in validating the model parameters across a range of temperatures, as the model parameters at all temperatures within the temperature range affect the simulated results.

Figure 4.5(a) plots the experimental temperature history, which ranges from 350° to 950° C. Figure 4.5(b) compares the experimental and simulated results by plotting the measured and simulated stress as a function of time. While the flow stress between the model and experiment does differ for the first few hundred cycles, the stabilized stress/mechanical strain hysteresis is quite similar. This comparison suggests the model captures the temperature dependence of Alloy 617 with sufficient accuracy for engineering design.

4.2.5 Pressurized SMT tests

The ART program developed the pressurized SMT test geometry to assess the combined effects of axial cycling, elastic follow up, and internal pressure/multiaxial load on the cyclic life of high temperature reactor materials. The program completed several tests of this kind for Alloy 617 at 950° C [24]. Comparing finite element simulation results using the Alloy 617 model to the experimental data validates the model for complex multiaxial loading conditions, representative of actual component service conditions.

Figure 4.6 shows the finite element model used to simulate the tests. The experimental thermomechanical loading consists of:

1. Constant, controlled, elevated temperature

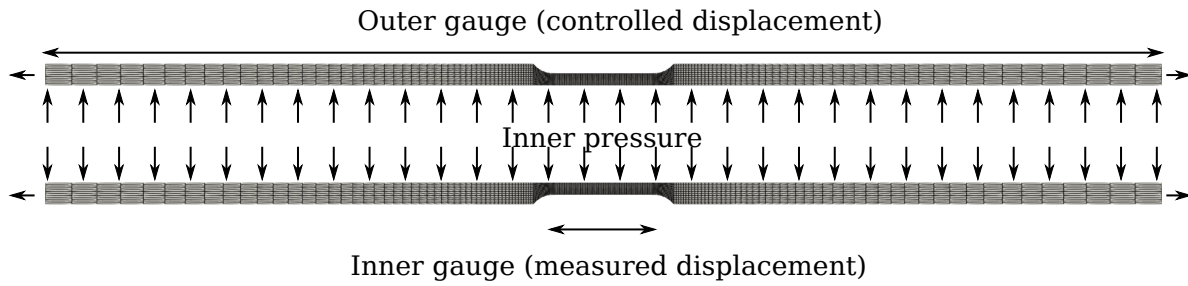


Figure 4.6: Sketch showing the p-SMT test geometry, loading, and the corresponding finite element model used here to compare the Alloy 617 material model to the experimental results.

2. Internal gas pressurization
3. Displacement loading, controlled with an extensometer, on the “outer bar” part of the specimen.

The experimental results are the load cell data, converted to the stress on the “inner bar” section and a second extensometer reading over the “inner bar” gauge, which can be converted to the axial strain over that region.

The experimental and the corresponding simulation results can be summarized by an axial stress/axial strain hysteresis diagram. This type of plot captures the key material behavior sampled by the test:

1. Elastic follow up during the hold
2. The effect of multiaxial load on the material stress/strain response
3. The effect of pressure, predominantly in the form of ratcheting (i.e. the hysteresis loop does not remain stable, but rather marches in either the tension or compression direction).

Figure 4.7 plots the model results in the form of hysteresis loops showing a particular load cycles, labeled on the plot. We compared the model and experiment for two different loading conditions. Both tests kept the temperature fixed to 950° C and imposed a 0.114 mm displacement on the outer bar. However, one test had an internal pressure of 2 psi while the other test had an internal pressure of 150 psi. Compared to the experimental data [24] the model captures the influence of pressure on the ratcheting rate and the follow up correctly. However, it does not

4.3 Model discrepancies

Overall, the Alloy 617 model developed here reasonably captures the material behavior as observed in the various experimental tests used to calibrate and validate the model.

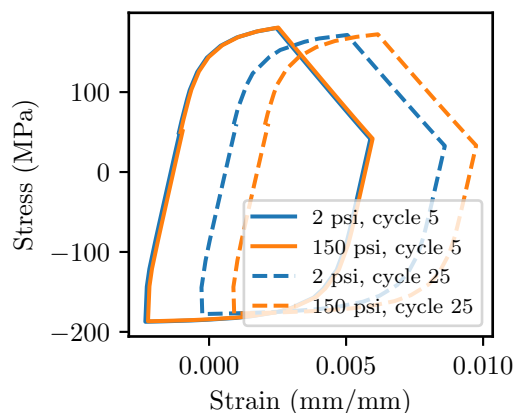


Figure 4.7: Pressurized SMT simulation data.

The largest differences between the model and the experiment are in the flow stress at intermediate temperatures (above room temperature but below 650° C) and at and above 950° C.

At high temperatures the material is essentially perfectly plastic. Figures 2.1 and 4.1 demonstrate that the model flow stress is about 20% less than the flow stress from the smoothed experimental data and the larger database of yield stress measurements. Section 2.4 explains this discrepancy in the original 950° C model. The discrepancy carries over to the full model. We view this difference as a combination of difficulties in controlling the strain rate of the material at very high temperatures, the strong rate sensitivity of Alloy 617 at high temperature, and a side effect of smoothing the tensile curves. The detailed comparison to the actual as-measured strain data (for example Figures 2.3-2.5) demonstrates that the model is sufficiently accurate at this temperature. The apparent inaccuracy in the flow stress is a consequence of testing at very high temperatures, leading to larger experiment-to-experimental measurement variations than would typically be expected for tensile and creep-fatigue test results and the challenge in controlling the strain rates at high temperatures, as discussed earlier.

In between room temperature and 650° C the model reports a somewhat higher flow stress than both the average of all data (as exemplified by Fig. 4.1) and higher than the dedicated fatigue tests (Fig. 3.6). However, the model matches the Alloy 617 Code Case tensile test results in this temperature range (Fig. 3.4) and falls within the scatter of the larger yield stress database (Fig. 4.1). This indicates that that original Code Case test campaign material material, used to calibrate the model flow stress, is somewhat stronger than the average Alloy 617. However, this effect is not significant as the model results still fall within the expected range of flow stress considering all heats. As such, both this discrepancy and the high temperature difference are acceptable and the model is suitable for use with the ASME design by inelastic analysis rules.

5 Conclusions

5.1 Summary of A617 modeling

This report described the development and validation of a complete inelastic constitutive model for Alloy 617, suitable for use with the design by inelastic analysis Section III, Division 5, Subsection HB, Subpart B ASME Boiler & Pressure Vessel Code rules for evaluating high temperature, Class A reactor components against the strain accumulation and creep-fatigue design limits. The model uses a standard Chaboche viscoplastic form at high temperatures, transitioning to a rate independent equivalent model at lower temperatures and faster strain rates. The model was calibrated against a detailed set of experiments at 950° C from the Alloy 617 Code Case qualification effort. Simple temperature scaling rules were then used to provide an all-temperature model with parameters covering the range from room temperature to 983° C. These temperature scaling rules were developed and calibrated against a smaller test database covering this larger range of temperatures.

We validated the model against a variety of experimental data not used in the calibration process. These validation comparisons include comparisons to a large number of abstracted experimental results as well as detailed comparisons to specialized tests. These specialized tests include examples of both non-isothermal and non-uniaxial load. Overall, this validation program meets the recommendations of the Nonmandatory Appendix Z to Subpart HBB of the ASME Code.

A few aspects of the model could be improved if additional experimental data becomes available. The model flow stress in the intermediate temperature range, above room temperature but less than 650° C may be somewhat higher than the average material. However, we do not have detailed tensile test data to assess this and the current model matches the available tests. The balance of isotropic and kinematic hardening could likewise be improved with additional cyclic testing. However, the model is sufficiently accurate to use for design with the ASME rules.

5.2 Balloting progress

We expect ASME to approve an initial version of the Nonmandatory Appendix Z sometime between July and November, 2021. This initial version includes general guidance on constructing constitutive models and a specific model for Grade 91, based on previous ART-sponsored work [2]. After this initial version is approved we will immediately begin balloting the second version. This revised version will add a model for 316H stainless steel [6] as well as the model for Alloy 617 described here. As the Alloy 617 material properties still reside in Nuclear Code Case 898, and not in the main code book, this new version will be split between a code change, targeting the 2023 edition of the ASME Code, and a revised Alloy 617 Code Case. When the Alloy 617 properties are merged into the main Code the inelastic model can be merged into the main Nonmandatory Appendix Z. Future work can then focus on developing models for the remaining three Class A materials: Alloy 800H, 304H stainless steel, and 2.25Cr-1Mo. The highest priority material, based on expected industry needs, is Alloy 800H.

Acknowledgments

The research was sponsored by the U.S. Department of Energy (DOE), under Contract No. DE-AC02-06CH11357 with Argonne National Laboratory, managed and operated by UChicago Argonne LLC, and Contract No. DE-AC07-05ID14517 with Idaho National Laboratory (INL), managed and operated by Battelle Energy Alliance LLC. Programmatic direction was provided by the Advanced Reactor Technologies (ART) Program of the Office of Nuclear Reactor Deployment of the Office of Nuclear Energy (NE). The authors gratefully acknowledge the support provided by Sue Lesica of DOE-NE, Federal Lead, ART Advanced Materials, Diana Li of DOE-NE, Federal Manager, ART Gas-Cooled Reactors (GCR) Campaign, and Gerhard Strydom of INL, National Technical Director, ART GCR Campaign.

The authors thank Yanli Wang of Oak Ridge National Laboratory for the p-SMT and thermomechanical test results and Bipul Barua of Argonne National Laboratory for helping with the p-SMT modeling.

Bibliography

- [1] A. K. Dhalla. Recommended practices in elevated temperature design: a compendium of breeder reactor experiences (1970-1987): Volume III - Inelastic analysis. Technical Report 366, 1991.
- [2] M. C. Messner and T.-L. Sham. Inelastic analysis procedure based on the Grade 91 unified viscoplastic constitutive model for ASME implementation. Technical report, Argonne National Laboratory, ANL-ART-167, Lemont, IL, 2019.
- [3] M. C. Messner, V.-T. Phan, and T.-L. Sham. FY17 Status Report on the Initial Development of a Constitutive Model for Grade 91 Steel. Technical report, Argonne National Laboratory, ANL-ART-93, OSTI 136734, Lemont, IL, 2017.
- [4] M. C. Messner, V.-T. Phan, and T.-L. Sham. A Unified Inelastic Constitutive Model for the Average Engineering Response of Grade 91 Steel. In *Proceedings of the 2018 ASME Pressure Vessels and Piping Conference*, pages PVP2018-84104. PVP2018-84104, 2018.
- [5] M. C. Messner, V.-T. Phan, and T.-L. Sham. Development of Grade 91 inelastic model for incorporation in ASME Division 5. Technical report, Argonne National Laboratory, ANL-ART-137, OSTI 146678, Lemont, IL, 2018.
- [6] M. C. Messner, V.-T. Phan, and T.-L. Sham. Development of the Technical Basis of a Unified Viscoplastic Model of 316H Stainless Steel for Incorporation into ASME Division 5. Technical report, Argonne National Laboratory, ANL-ART-166, Lemont, IL, 2019.
- [7] V.-T. Phan, M. C. Messner, and T.-L. Sham. A Unified Engineering Inelastic Model for 316H Stainless Steel. In *Proceedings of the 2019 ASME Pressure Vessels and Piping Conference*, 2019.
- [8] M. C. Messner and T.-L. Sham. Initial High Temperature Inelastic Constitutive Model for Alloy 617. Technical report, Argonne National Laboratory, ANL-ART-195, 2020.
- [9] T.-L. Sham and Kevin P. Walker. Preliminary Development of a Unified Viscoplastic Constitutive Model for Alloy 617 With Special Reference to Long Term Creep Behavior. In *Fourth International Topical Meeting on High Temperature Reactor Technology, Volume 2, Materials and Components*, pages 81–89. American Society of Mechanical Engineers, New York, NY, 2008.
- [10] J. L. Chaboche and G. Cailletaud. On the calculation of structures in cyclic plasticity or viscoplasticity. *Computers and Structures*, 23(1):23–31, 1986. ISSN 00457949. doi: 10.1016/0045-7949(86)90103-3.
- [11] J. L. Chaboche. Time-independent constitutive theories for cyclic plasticity. *International Journal of Plasticity*, 2(2):149–188, 1986. ISSN 07496419. doi: 10.1016/0749-6419(86)90010-0.

- [12] J. L. Chaboche. On some modifications of kinematic hardening to improve the description of ratchetting effects. *International Journal of Plasticity*, 7(7):661–678, 1991. ISSN 07496419. doi: 10.1016/0749-6419(91)90050-9.
- [13] J. L. Chaboche. A review of some plasticity and viscoplasticity constitutive theories. *International Journal of Plasticity*, 24(10):1642–1693, oct 2008. ISSN 07496419. doi: 10.1016/j.ijplas.2008.03.009. URL <http://linkinghub.elsevier.com/retrieve/pii/S0749641908000582>.
- [14] Adam Paszke, Sam Gross, Francisco Massa, Adam Lerer, James Bradbury, Gregory Chanan, Trevor Killeen, Zeming Lin, Natalia Gimelshein, Luca Antiga, Alban Desmaison, Andreas Kopf, Edward Yang, Zachary DeVito, Martin Raison, Alykhan Tejani, Sasank Chilamkurthy, Benoit Steiner, Lu Fang, Junjie Bai, and Soumith Chintala. PyTorch: An Imperative Style, High-Performance Deep Learning Library. In *Advances in Neural Information Processing Systems 32*, pages 8024—8035, 2019.
- [15] Ronald M. Errico. What Is an Adjoint Model? *Bulletin of the American Meteorological Society*, 78(11):2577–2591, 1997. ISSN 00030007. doi: 10.1175/1520-0477(1997)078<2577:WIAAM>2.0.CO;2.
- [16] ASTM International. E 21-09: Standard Test Methods for Elevated Temperature Tension Tests of Metallic Materials, 2009.
- [17] Walter Osthoff, Hans Schuster, Philip J. Ennis, and Hubertus Nickel. Creep and relaxation behavior of Inconel-617. *Nuclear Technology*, 66(2), 1984. ISSN 00295450. URL http://www.osti.gov/energycitations/product.biblio.jsp?osti_id=6469226.
- [18] U F Kocks. Realistic constitutive relations for metal plasticity. *Materials Science and Engineering A*, 317:181–187, 2001.
- [19] H Mecking, B Nicklas, N. Zarubova, and U F Kocks. A "universal" temperature scale for plastic flow. *Acta Metallurgica*, 34(3):527–535, 1986.
- [20] M C Messner, V Phan, and T Sham. Evaluating and modeling rate sensitivity in advanced reactor structural materials : 316H , Gr . 91 , and A617. *International Journal of Pressure Vessels and Piping*, 178:103997, 2019. ISSN 0308-0161. doi: 10.1016/j.ijpvp.2019.103997. URL <https://doi.org/10.1016/j.ijpvp.2019.103997>.
- [21] F. A. Leckie and D. R. Hayhurst. Creep rupture of structures. *Proceedings of the Royal Society A: Mathematical, Physical and Engineering Sciences*, 340:323–347, 1974. ISSN 1364-5021. doi: 10.1098/rspa.1983.0054.
- [22] F. A. Leckie and D. R. Hayhurst. Constitutive equations for creep rupture. *Acta Metallurgica*, 25(9):1059–1070, 1977. ISSN 00016160. doi: 10.1016/0001-6160(77)90135-3.
- [23] D. R. Hayhurst, F. A. Leckie, and J. T. Henderson. Design of notched bars for creep-rupture testing under tri-axial stresses. *International Journal of Mechanical Sciences*, 19(3):147–159, 1977.

- [24] Y. Wang, R. I. Jetter, and T.-L. Sham. Effect of Internal Pressurization on the Creep-Fatigue Performance of Alloy 617 Based on Simplified Model Test Method. In *Proceedings of the ASME 2019 Pressure Vessels & Piping Conference*, pages PVP2019–93650, 2019.

A Description of A617 and 316H material models for the ASME Appendix Z

The Alloy 617 design data resides in a Nuclear Code Case (N-898) whereas the main Appendix Z, with the models for Grade 91, 316H, and the rest of the materials, will reside in the main Section III, Division 5. The Alloy 617 model will need to be added to a revised Code Case N-898, as the main Code cannot reference a Code Case. As such, the following description of the 316H and A617 models, intended to form the basis of an action at ASME adding the two materials to the Appendix Z, splits out the models into separate subsections. The description of the 316H model comes from our past work [6, 7], the current report describes the A617 model.

A.1 316H

Tables A.1 and A.2 define the symbols used in the mathematical equations defining the model.

The model is defined by four ordinary differential equations:

$$\dot{\boldsymbol{\sigma}} = (1 - \omega) \mathbf{C} : (\dot{\boldsymbol{\epsilon}} - \dot{\boldsymbol{\epsilon}}_{vp} - \alpha \dot{T} \mathbf{I}) \quad (\text{A.1})$$

$$\dot{K} = \delta (R - K) \dot{\gamma} \quad (\text{A.2})$$

$$\dot{\mathbf{X}}_i = \left(\frac{2}{3} C_i \frac{\partial f}{\partial \boldsymbol{\sigma}} - \sqrt{\frac{2}{3}} \gamma_i \mathbf{X}_i \right) \dot{\gamma} \quad (\text{A.3})$$

$$\dot{\omega} = \frac{1}{(1 - \omega)^\phi} \left(\frac{\sigma_{vm}}{\sigma_0} \right)^\xi \quad (\text{A.4})$$

with two backstresses, i.e. $i = 1, 2$. \mathbf{C} is the isotropic elasticity tensor defined by the values of the Young's modulus E and Poisson's ratio ν given in Table A.2. These values match the values provided in Section II, Part D for Alloy 617. Similarly, Table A.2 lists the values of the instantaneous coefficient of thermal expansion α , which match the values in Section II, Part D.

The viscoplastic strain rate is

$$\dot{\boldsymbol{\epsilon}}_{vp} = \sqrt{\frac{3}{2}} \left\langle \frac{f(\boldsymbol{\sigma} - \mathbf{X}) - \sigma_0 - \sqrt{\frac{2}{3}} K}{\sqrt{2/3} \eta} \right\rangle^n \frac{\partial f}{\partial \boldsymbol{\sigma}} \quad (\text{A.5})$$

with

$$f = \sqrt{\frac{3}{2}} (\mathbf{s} - \mathbf{X}) : (\mathbf{s} - \mathbf{X}) \quad (\text{A.6})$$

and

$$\mathbf{X} = \sum_{i=1}^{n_{back}} \mathbf{X}_i. \quad (\text{A.7})$$

Table A.2 defines the parameter values as a function of temperature. The parameters may be linearly interpolated between the values listed in the table.

Symbol	Description
$\dot{\boldsymbol{\sigma}}$	Stress rate
$\boldsymbol{\sigma}$	Stress
$\dot{\boldsymbol{\epsilon}}$	Total strain rate
\dot{K}	Isotropic hardening rate
K	Value of isotropic hardening
$\dot{\mathbf{X}}_i$	Backstress evolution rate
\mathbf{X}_i	Value of the backstress
$\dot{\omega}$	Damage parameter rate
ω	Damage parameter
\dot{T}	Temperature rate
T	Temperature
α	Instantaneous coefficient of thermal expansion
\mathbf{C}	Isotropic elasticity tensor
f	Flow function
$\partial f / \partial \boldsymbol{\sigma}$	Derivative of the flow function with respect to the stress
\mathbf{I}	Rank 2 identity tensor
$\dot{\gamma}$	Consistency parameter
\mathbf{s}	Stress deviator, $\mathbf{s} = \boldsymbol{\sigma} - \frac{1}{3} \text{tr}(\boldsymbol{\sigma}) \mathbf{I}$
\mathbf{X}	Total back stress
σ_0	Threshold stress

Table A.1: Definition of mathematical symbols used to define the 316H model.

Parameter	Units	25° C	427° C	550° C	600° C	650° C	700° C	815° C
E	MPa	195,000	166,840	156,000	151,000	146,000	140,000	126,200
ν	-	0.31	0.31	0.31	0.31	0.31	0.31	0.31
α	$\frac{\text{mm/mm}}{^{\circ}\text{C}}$	1.54×10^{-5}	1.96×10^{-5}	2.06×10^{-5}	2.11×10^{-5}	2.16×10^{-5}	2.17×10^{-5}	1.89×10^{-5}
η	MPa	260.21	122.00	113.52	228.09	264.89	329.67	255.39
n	-	19.419	19.011	15.842	9.2861	8.8989	7.9975	7.9000
σ_0	MPa	32.792	39.182	29.353	7.4851	16.074	13.961	12.000
R	MPa	20.808	214.05	158.00	153.90	71.460	71.317	1.0000
δ	-	7.1487	1.1807	1.0421	1.9878	4.4547	3.3879	0.01000
C_1	MPa	6111.5	7385.8	26960	15118	5028.3	1612.0	106.46
γ_1	-	416.45	480.68	506.44	309.63	89.906	12.092	2.5278
C_2	MPa	20167	7385.8	2925.6	2782.8	3980.9	6080.3	9946.9
γ_2	-	165.57	93.685	10.256	18.237	120.46	311.97	150.53
σ_0	MPa	32035	6269.8	3767.5	2804.9	2174.0	1722.4	1180.5
ξ	-	20.619	8.2140	7.2670	6.5517	6.1535	5.7778	5.1900
ϕ	-	1.5000	1.5000	1.1149	1.7100	1.2227	1.5000	1.5000

Table A.2: 316H model parameters. Units are compatible with megapascals for stress, Celsius for temperature, and seconds for time.

Symbol	Description
$\dot{\boldsymbol{\sigma}}$	Stress rate
$\boldsymbol{\sigma}$	Stress
$\dot{\boldsymbol{\epsilon}}$	Total strain rate
\dot{K}	Isotropic hardening rate
K	Value of isotropic hardening
$\dot{\mathbf{X}}_i$	Backstress evolution rate
\mathbf{X}_i	Value of the backstress
$\dot{\omega}$	Damage parameter rate
ω	Damage parameter
\dot{T}	Temperature rate
T	Temperature
α	Instantaneous coefficient of thermal expansion
\mathbf{C}	Isotropic elasticity tensor
f	Flow function
$\partial f / \partial \boldsymbol{\sigma}$	Derivative of the flow function with respect to the stress
\mathbf{I}	Rank 2 identity tensor
$\dot{\gamma}$	Consistency parameter
σ_{vm}	von Mises stress, $\sigma_{vm} = \sqrt{\frac{3}{2} \mathbf{s} : \mathbf{s}}$
\mathbf{s}	Stress deviator, $\mathbf{s} = \boldsymbol{\sigma} - \frac{1}{3} \text{tr}(\boldsymbol{\sigma}) \mathbf{I}$
g	Normalized activation energy
\mathbf{X}	Total back stress
σ_0	Threshold stress

Table A.3: Definition of mathematical symbols used to define the Alloy 617 model.

A.2 Alloy 617

Tables A.3 and A.4 provide the definition of each symbol in the equations defining the Alloy 617 material model.

The model is an ordinary differential equation defined by four rate equations:

$$\dot{\boldsymbol{\sigma}} = (1 - \omega) \mathbf{C} : \left(\dot{\boldsymbol{\epsilon}} - \dot{\gamma} \frac{\partial f}{\partial \boldsymbol{\sigma}} - \alpha \dot{T} \mathbf{I} \right) \quad (\text{A.8})$$

$$\dot{K} = \delta (R - K) \dot{\gamma} \quad (\text{A.9})$$

$$\dot{\mathbf{X}}_i = \left(\frac{2}{3} C_i \frac{\partial f}{\partial \boldsymbol{\sigma}} - \sqrt{\frac{2}{3}} \gamma_i \mathbf{X}_i \right) \dot{\gamma} \quad (\text{A.10})$$

$$\dot{\omega} = \frac{1}{(1 - \omega)^\phi} \left(\frac{\sigma_{vm}}{\sigma_0} \right)^\xi \quad (\text{A.11})$$

where the 617 model has three backstresses, i.e. $i = 1, 2, 3$.

The model switches between a rate sensitive and rate insensitive response based on the

Kocks-Mecking normalized activation energy. This switch affects the definition of the consistency parameter:

$$g = \frac{kT}{\mu b^3} \log \frac{\dot{\epsilon}_0}{\sqrt{2/3 \dot{\epsilon} : \dot{\epsilon}}} \quad (\text{A.12})$$

$$\dot{\gamma} = \begin{cases} \dot{\gamma}_{ri} & g \leq g_0 \\ \dot{\gamma}_{rd} & g > g_0 \end{cases}. \quad (\text{A.13})$$

The consistency parameter in the rate independent regime is given by the standard rate independent flow theory defined by the Kuhn-Tucker conditions:

$$\dot{\gamma}_{ri} > 0 \quad (\text{A.14})$$

$$f \leq 0 \quad (\text{A.15})$$

$$\dot{\gamma}_{ri} f = 0 \quad (\text{A.16})$$

$$\dot{\gamma}_{ri} \dot{f} = 0. \quad (\text{A.17})$$

In the rate dependent regime the consistency parameter is given by the viscoplastic power law

$$\dot{\gamma}_{rd} = \frac{\langle f \rangle^n}{\eta}. \quad (\text{A.18})$$

For both cases the flow direction and the consistency parameter are defined in terms of the flow function, which uses standard J_2 /von Mises flow theory

$$f = \sqrt{\frac{3}{2} (\mathbf{s} - \mathbf{X}) : (\mathbf{s} - \mathbf{X})} - (\sigma_0 + K) \quad (\text{A.19})$$

with \mathbf{X} the total backstress

$$\mathbf{X} = \sum_{i=1}^3 \mathbf{X}_i \quad (\text{A.20})$$

\mathbf{s} the stress deviator

$$\mathbf{s} = \boldsymbol{\sigma} - \frac{1}{3} \text{tr}(\boldsymbol{\sigma}) \mathbf{I} \quad (\text{A.21})$$

where $\boldsymbol{\sigma}$ is the stress and

$$\sigma_0 = \begin{cases} \sigma_y & g \leq g_0 \\ 0 & g > g_0 \end{cases}. \quad (\text{A.22})$$

Table A.4 and the following equations define the parameters used in the mathematical definition of the model as a function of temperature. The units are consistent with MPa for stress, °C for temperature, and seconds for time.

Elasticity and thermal expansion

\mathbf{C} is the isotropic elasticity tensor defined by the temperature-dependent values of the Young's modulus E and Poisson's ratio ν given in Code Case N-898 for Alloy 617. α denotes the value of the instantaneous thermal expansion coefficient, likewise given in Code Case N-898.

Symbol	Description	Value
E	Young's modulus	Values in ASME Code Case N-898 (MPa)
ν	Poisson's ratio	Values in ASME Code Case N-898
α	Instantaneous coefficient of thermal expansion	Values in ASME Code Case N-898 (mm/mm/K)
k	Boltzmann constant	1.38064×10^{-20} kJ/K
b	Burgers vector	2.474×10^{-7} mm
$\dot{\epsilon}_0$	Reference strain rate	10^{10} 1/s
A_{km}	Kocks-Mecking slope	-7.985
B_{km}	Kocks-Mecking intercept	-0.6696
C_{km}	Kocks-Mecking horizontal asymptote	-5.550
g_0	Kocks-Mecking intersection point	0.6112
C_{lm}	Larson-Miller parameter	9.666
A_{lm}	Larson-Miller slope	26779
B_{lm}	Larson-Miller intercept	-4676.9
ϕ	Hayhurst-Leckie shape constant	1.8
C_1	Backstress 1 hardening rate	643.933 MPa
C_2	Backstress 2 hardening rate	40.3267 MPa
C_3	Backstress 3 softening rate	-20.600 MPa
γ_1	Backstress 1 dynamic recovery	103.7
γ_2	Backstress 2 dynamic recovery	5.089
γ_3	Backstress 3 dynamic recovery	0.9823

Table A.4: A617 model parameters. Units are compatible with megapascals for stress, Celsius for temperature, and seconds for time.

Rate sensitivity and initial flow stress

$$\mu = \frac{E}{2(1 + \nu)} \quad (\text{A.23})$$

$$\sigma_y = \mu e^{C_{km}} \quad (\text{A.24})$$

$$n = \frac{-\mu b^3}{k(T + 273.15) A_{km}} \quad (\text{A.25})$$

$$\eta = e^{B_{km}} \mu \dot{\epsilon}_0^{-1/n} \quad (\text{A.26})$$

Damage model

$$\xi = -\frac{B_{lm}}{T + 273.15} \quad (\text{A.27})$$

$$\sigma_0 = \frac{10^{C_{lm}(T+273.15)/B_{lm} - A_{lm}/B_{lm}}}{(\phi + 1)^{(T+273.15)/B_{lm}}}. \quad (\text{A.28})$$

Isotropic hardening

$$R = \begin{cases} 0.70 (-9.778 \times 10^{-4} (T + 273.15)^2 + 1.161 (T + 273.15) + 88.93) & T < 750^\circ \text{ C} \\ -3.546 ((T + 273.15) - 1023.15) + 177.3 & 750^\circ \text{ C} \leq T < 800^\circ \text{ C} \\ -0.1182 ((T + 273.15) - 1073.15) & 800^\circ \text{ C} \leq T < 950^\circ \text{ C} \\ -17.73 & T \geq 950^\circ \text{ C} \end{cases} \quad (\text{A.29})$$

$$\delta = \begin{cases} \frac{0.04\mu}{R} & T < 750^\circ \text{ C} \\ -0.06228188T + 60.145026 & 750^\circ \text{ C} \leq T < 800^\circ \text{ C} \\ 10.32 & T \geq 800^\circ \text{ C} \end{cases} \quad (\text{A.30})$$



Applied Materials Division

Argonne National Laboratory
9700 South Cass Avenue, Bldg. 212
Argonne, IL 60439

www.anl.gov



**U.S. DEPARTMENT OF
ENERGY**

Argonne National Laboratory is a U.S. Department of Energy
laboratory managed by UChicago Argonne, LLC